



DESIGN AND IMPLEMENTATION OF INTRAVASCULAR  
HIFU CATHETER ABLATION SYSTEM

by  
OMID FARHANIEH

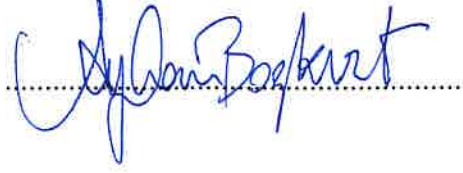
Submitted to the Graduate School of Engineering and Natural Sciences  
in partial fulfillment of  
the requirements for the degree of  
Doctor of Philosophy

Sabancı University  
July 2018

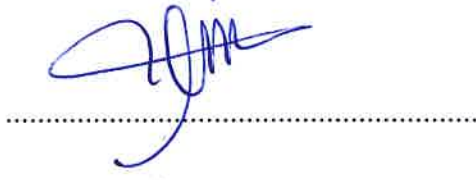
DESIGN AND IMPLEMENTATION OF INTRAVASCULAR HIFU  
CATHETER ABLATION SYSTEM

APPROVED BY:

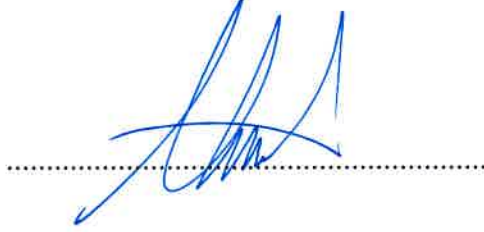
Associate Professor, Dr. Ayhan Bozkurt  
(Thesis Supervisor)



Prof. Dr. İbrahim Tekin



Assoc. Prof. Dr. Ahmet Onat



Assoc. Prof. Dr. Arif Sanlı Ergün



Assoc. Prof. Dr. Gökseven Yaralıoğlu



DATE OF APPROVAL: 20/07/2018

© Omid Farhanieh 2018

All Rights Reserved

## ABSTRACT

### DESIGN AND IMPLEMENTATION OF INTRAVASCULAR HIFU CATHETER ABLATION SYSTEM

OMID FARHANIEH

Ph.D. Dissertation, July 2018

Supervisor: Assoc. Prof. Dr. Ayhan Bozkurt

**Keywords:** High-intensity focused ultrasound, HV-CMOS HIFU transmitter IC, CMUT-based HIFU catheter, Phase locked loop

High-intensity focused ultrasound is an energy-based thermal therapy for non-invasive or minimally invasive treatment of wide range of medical disorders including solid cancer tumors, brain surgery, atrial fibrillation (AF) and other cardiac arrhythmias. Conventional HIFU is extracorporeally administered but in applications where a small lesion or more precise energy localization in shorter time is required, catheter-based HIFU devices which are positioned directly within or adjacent to the target may be the best solution.

Available HIFU catheters use array of piezoelectric transducers with complex external high-voltage (HV) and high-frequency amplifiers, a cooling system and several coaxial cables within the catheter. In this study, a HV transmitter IC has been designed, manufactured and integrated with an 8-element capacitive micromachined ultrasound transducer (CMUT) on a prototype HIFU probe appropriate for a 6-Fr catheter. The transmitter IC fabricated in 0.35  $\mu\text{m}$  HV CMOS process and comprises eight continuous-wave HV buffers (10.9 ns and 9.4 ns rise and fall times at 20  $V_{pp}$  output into a 15 pF), an eight-channel transmit beamformer (8-12 MHz output frequency with 11.25 ° phase accuracy) and a phase locked loop with an integrated VCO as a tunable clock source (128–192 MHz). The chip occupies 1.85 $\times$ 1.8 mm<sup>2</sup> area including input and output (I/O) pads. Electrical measurements, IR thermography and Ex-vivo experiment results reveal that the presented HIFU system can elevate the temperature of the target region of tissue around 19 °C by delivering 600 CEM<sub>43</sub> equivalent thermal dose while surface temperature of the probe rises less than 5 °C.

## ÖZET

### İNTRAVASKÜLER HIFU CATHETER ABLASYON SİSTEMİ TASARIMI VE GERÇEKLENMESİ

OMID FARHANIEH

Doktora tezi, Temmuz 2018

Danışman: Doç. Dr. Ayhan Bozkurt

**Anahtar Kelimeler:** Yüksek yeğinlikli odaklanmış ultrason, yüksek gerilim HIFU sürme tümleşik devresi, CMUT tabanlı HIFU kateteri, faz kilitlemeli döngü

Yüksek yeğinlikli odaklanmış ultrason (High-intensity focused ultrasound - HIFU), katı urlar, kulakçık fibrilasyonu ve benzeri kardiyak aritmiler gibi çok sayıda tıbbi rahatsızlığın sağaltımında ve beyin cerrahisinde kullanılan enerji tabanlı bir non-invazif veya minimal invazif ısıl terapi yöntemidir. Geleneksel HIFU vücut dışından uygulanmakla beraber, göreceli küçük lezyon oluşturulması veya kısa sürede yüksek enerji biriktirilmesi gereken durumlarda hedef dokunun içine veya yanına konumlandırılabilen kateter tabanlı cihazların kullanımı en iyi sonuçları sağlamaktadır.

Var olan kateter tabanlı HIFU cihazları, piezoelektrik dönüştürücü dizinleri kullanmakta, karmaşık yüksek-gerilim ve yüksek-frekans güç yükselticileri, soğutma sistemleri ve kateter içine yerleştirilmiş çok sayıda koaksiyel kablo gerektirmektedir. Bu çalışmada, 6-Fr çapında prototip bir HIFU kateteri için bir yüksek gerilim sürme tümleşik devresi tasarlanmış ve üretilmiş, devre 8 ögeli bir kapasitif mikroişlenmiş ultrason dönüştürücü (CMUT) dizini ile tümleştirilmiştir. Yüksek gerilim 0.35  $\mu\text{m}$  CMOS süreci ile üretilen tümleşik devre, 15 pF yük ve 20 V<sub>pp</sub> çıkış gerilimi için 10.9 ns yükselme ve 9.4 ns düşme süresine sahip sekiz adet sürekli zaman sürme tamponu, 8-12 MHz çalışma frekanslı ve 11.25° faz çözünürlüklü sekiz kanallı sürme huzmesi oluşturucu ve 128-192 MHz'lik tümleşik VCO'lu PLL tabanlı saat işareti kaynağı içermektedir. Tümleşik devre, giriş-çıkış tamponlarıyla birlikte 1.85×1.8 mm<sup>2</sup> kırmık alanına sahiptir. Elektriksel ölçümler, kızılaltı termografi ve canlı dışı deneyler, sunulan HIFU sisteminin hedef dokuya 600 CEM<sub>43</sub> eşdeğer ısıl doz uygulayarak sıcaklığı 19° C attırabildiğini, bu sırada kateter yüzeyindeki sıcaklık artışının 5° C'nin altında kaldığını göstermiştir.

*To the memory of my **father***

## ACKNOWLEDGEMENTS

First and foremost, I would like to express my deepest gratitude to my advisor, Dr. Ayhan Bozkurt for his support and encouragement throughout my Ph.D. Words cannot even begin to describe his great support and the impression that working with him has left upon me. With his mastery of a vast number of subject matters, as an advisor, a mentor, and a friend, he has had a tremendous influence on both my professional and personal development. I thoroughly enjoyed every single day of my Ph.D. working with him. I am also deeply indebted to him for his unlimited supports, always positive behavior, kindness and friendship in these years. He always treats as a leader and works closely along with students in lab and in support of their simulation works as well. I could not have imagined having a better mentor for my Ph.D.

My sincere appreciation is extended to other committee members, Assoc. Prof. Dr. Arif Sanlı Ergün, Prof. İbrahim Tekin, Assoc. Prof. Dr. Göksenin Yaralıoğlu and Assoc. Prof. Dr. Ahmet Onat for serving on my candidacy and thesis committees and for their suggestions, questions and comments. My special gratitude to Professor Sanlı Ergün for his valuable helps during the HIFU catheter project; I have learned a lot in the experiments and technical discussions with you. My other special gratitude to Professor Yaralıoğlu and Professor Onat for their support during the “hand-held imaging probe” and “SWARMS” project respectively. I would also like to thank Professor Tekin and his former PhD Student, Dr. Mirmehdi Seyyedefahlan, for their assistance in my chip measurements.

I feel very lucky to have worked with the current and former teammates at Acoustics group of Sabancı University. Dr. Rupak Bardhan Roy, Reza Pakdaman, Mansoor Ahmad and Muhammad Omer Asim. Without Rupak’s masterly fabricated CMUT devices this work would not have been successful. Reza also helped me making one of the best decisions of my life in joining to Dr. Bozkurt’s group. Special thanks to Dr. Ali Sahafi, my great friend, mentor and brother for his helps during my thesis. I would also like to acknowledge former and current lab specialists of electronics engineering group at Sabancı University, Mehmet Doğan and Ali Kasal for their patience and supports.

I would like to deeply thank my family for all their loves and supports. My mom and my deceased dad have supported me so much, so I could be where I am today. My

full of love thanks to my sisters Souzan, Mojgan, and my brother Ebrahim for their supports. Beginning of my Ph.D. coincided with my father's terminal stage illness which eventually claimed his life after two difficult years. During those years, all supports, sacrifices and encouragements of my mom, my sister, Souzan, and her family, Hasan, Arash, Armin and kindness of my respected relatives, especially my kind cousin Leyla, made it possible for me to complete this work abroad. I would also like to express my gratitude to my parents-in-law for all their supports, understandings and sacrifices that they have made for us.

Finally and most importantly, I would like to express my deepest gratitude and love to my wonderful wife, Fereshteh, whose unlimited love, encouragement and patience has been the greatest source of energy for me to keep going forward during the entire of my M.Sc. and Ph.D. Nothing would have ever been possible without your endless support and love. Thank you for being my best friend.

# TABLE OF CONTENT

Chapter 1 Introduction to High-Intensity Focused Ultrasound.....	1
1.1 Physical Principles of HIFU.....	2
1.2 Medical Considerations of HIFU .....	5
1.3 Main Components of HIFU System.....	6
1.4 Research Objectives.....	7
1.5 Organization of Dissertation .....	9
Chapter 2 Overview of HIFU Systems.....	11
2.1 Existing HIFU systems .....	11
2.2 Catheter-based HIFU devices .....	12
2.3 CMUT based HIFU catheters.....	13
Chapter 3 Design of Integrated HIFU Catheter System.....	17
3.1 Block-level Specifications .....	17
3.1.1 Digital Pulse Generator and Phase Locked Loop.....	18
3.1.2 Analog Pulse Generator.....	19
3.1.3 Continuous-Wave Eight-Channel High-Voltage Driver Requirements based on Characterization of CMUT Arrays .....	19
3.2 Safe Operating Region for The Integrated HIFU Catheter .....	22
Chapter 4 HIFU Transmitter IC Design and Implementation.....	27
4.1 Digital Pulse Generator.....	27
4.2 Phase Locked Loop.....	29
4.2.1 Capacitive-Tuned Ring VCO .....	30
4.2.2 Phase/Frequency Detector and Charge Pump .....	33
4.2.3 Frequency Divider.....	35
4.3 High Voltage Driver Array .....	36
4.4 Analog Pulse generator .....	38

4.4.1	Differential Ring VCO .....	39
4.4.2	Loop Filter .....	40
Chapter 5	Chip Measurement and HIFU System Characterization .....	42
5.1	Phase Locked Loop .....	43
5.2	Digital Pulse Generator .....	44
5.3	High Voltage Driver.....	45
5.4	8-12 MHz PLL and Analog Pulse generator.....	47
5.5	Real-Time HIFU Beam Thermography .....	49
5.6	<i>Ex-Vivo</i> Experiments on Ovine Liver .....	52
5.7	Self-heating Assessment of Catheter Surface .....	54
Chapter 6	CONCLUSION AND FUTURE WORK .....	57
REFERENCES	.....	59

# LIST OF FIGURES

Figure 1.1: Heating a target spot with focused energy: (a) Sunrays, (b) Ultrasound beam.....	1
Figure 1.2: Drawing of spherically curved transducer and its focusing cigar-shaped beam pattern with diameter of $d_r$ and length of $d_z$ .....	4
Figure 1.3: Different methods of ultrasound wave focusing: a) Flat transducer and interchangeable lens, b) Curved transducer with constant focal point, c) Phased-array transducer without focusing, d) Phased-array transducer with adjustable focusing.....	6
Figure 1.4: Conceptual drawing of HIFU Catheter Ablation System. The radial distance of the ablation spot will be set by the phase of the individual drive pulses applied to the elements of the ring array .....	8
Figure 1.5: Microscope image of the 8-element concentric array used for the catheter ablation system. Each of the 8 elements of the array have equal area. Cell diameter is 44 $\mu\text{m}$ . The device was fabricated on a highly conducting Si substrate using surface micromachining techniques. While the membrane material is PECVD $\text{Si}_3\text{N}_4$ , Au/Cr is used as the electrode material. ....	9
Figure 2.1: Some of commercial HIFU systems: (a) Sonablate <sup>®</sup> , (b) Ablatherm <sup>®</sup> , (c) Sonatherm <sup>®</sup> .....	11
Figure 2.2: Some of available catheter-based HIFU devices: (a) A bi-directional endocervical HIFU catheter for treatment of locally advanced cervical carcinoma [39]. (b) 7-sided interstitial device for brain ablation by Carthera [36]. (c) Transballoon HIFU catheter developed by Johnson & Johnson for atrial fibrillation treatment [38].....	13
Figure 2.3: CMUT-based ten facets HIFU catheter prototype [46]. ....	15
Figure 3.1: Block diagram of HIFU system with the first chip. All functional blocks of a complete array driver, which include a PLL with an integrated VCO, a digital pulse generator, and HV drivers are combined on a single chip.....	18
Figure 3.2: Block diagram of HIFU system with the second chip. The trigger pulse generator integrated in an 8-12 MHz PLL.....	19
Figure 3.3: Impedance measurement of a CMUT element: (a) Wire-bonded device to PCB, (b) coated with two-part epoxy for protection of wires, (c) measured impedance of one element when the device is immersed in oil.....	21

Figure 3.4: FEM model of catheter tip used in thermal simulations. The axisymmetric model assumes that the IC is placed on a silver block and encapsulated in a low thermal conductivity epoxy layer. The entire model is stationary; cooling effect of blood flow is not included. ....	23
Figure 3.5: FEM simulation result of temperature transient at the catheter surface while the IC is dissipating 500 mW of power. The temperature exceeds safety limits after 100 seconds.....	24
Figure 3.6: FEM simulation result showing the generated pressure at 96 $\mu\text{m}$ distance from the surface of the CMUT used in the HIFU system. The transducer is biased at 130 Volts DC and driven with 20 V <sub>pp</sub> amplitude at 10 MHz. The RMS pressure is 395 kPa.....	25
Figure 3.7: Simulation result of temperature generated by the CMUT ring array at a focal distance of 4 mm. A temperature rise of 19 °C is anticipated in 11 seconds. 26	26
Figure 4.1: Geometry of the transducer array used in experiments.....	28
Figure 4.2: One channel of the digital beamformer. Two parallel loadable synchronous counters generate 50% duty cycle pulses, whose overlap can be adjusted by the initial count value to set the duty cycle of the output. The XOR gates acting as programmable inverters provide an additional half clock cycle phase resolution. PH and PL, which are always 180° out of phase, provide the drive signals for the PMOS and NMOS of the output driver, respectively. All data are shifted in serially.....	29
Figure 4.3: Functional block diagram of Integer-N PLL, which comprises a phase and frequency detector, and charge pump, the loop filter, a VCO, and a programmable divider. ....	30
Figure 4.4: Simplified schematic of proposed ring VCO. While six out of nine inverters are loaded with variable capacitors, one has a fixed output capacitor to set the tuning range. ....	31
Figure 4.5: Measurement result for the open-loop VCO gain within the tuning range. To account for process corner variations, the tuning range is kept slightly larger than the desired range of 128–192 MHz.....	32
Figure 4.6: Gate-level schematic of Nand-based phase and frequency detector .....	33
Figure 4.7: Circuit schematic of the charge pump, with M <sub>FP</sub> and M <sub>FN</sub> feedback transistors added to compensate the up and down current mismatch. ....	34

Figure 4.8: Normalized current error of charge pump circuit. Feedback reduces the error up to 60% within the tuning range.....	34
Figure 4.9: Schematic of frequency divider.....	35
Figure 4.10: Circuit schematic of proposed High-Voltage pulser. Pulse_L and Pulse_H signals, which are generated by the digital beamformer, pass through super buffers to be able to drive the large sized output transistors.....	36
Figure 4.11: Layout view of single HV driver cell.....	37
Figure 4.12: The differential ring VCO used in transmit beamforming circuit for one channel. Any of the 16 generated signals by VCO can be fed to the HV driver. Duty-cycle of non-overlap PH and PL can be adjusted by appropriate combination of the VCO outputs. ....	38
Figure 4.13: Schematic of single delay cell used in VCO. A pair of 500 fF capacitors at outputs of each cell are used to decrease the phase errors due to non-equal routes of output clocks. ....	39
Figure 4.14: Post-layout simulation result of delay-cell based fully differential ring VCO.....	40
Figure 4.15: Conceptual (left) and circuit schematic (right) of capacitor multiplier.....	41
Figure 4.16: Frequency response of low-pass low-pass filter: with ideal 2.4 nF capacitor (red), with 20×120 pF capacitor multiplier (blue). The circuit designed for operation between 0.1-10 KHz, appropriate for the loop filter function. ....	41
Figure 5.1: Micrograph of the two manufactured driver ICs. HIFU transmitter IC with 128-192 MHz PLL as reference clock generator, digital trigger pulse generator, 8-element HV driver array (Left). 8-12 MHz Analog pulse generator and 8-element HV driver array (Right). ....	42
Figure 5.2: Step response of PLL seen from control voltage node of VCO.....	43
Figure 5.3: Output spectrum of PLL when locked at 128 MHz. ....	43
Figure 5.4: Phase noise of PLL locked at 128 MHz. ....	44
Figure 5.5: Measured PH and PL output for the 1st and 5th channels of the digital beamformer at 10 MHz. PH and PL are internal signals of the IC, but they are brought out on the prototype IC for test purposes. The duty cycle is 30%. ....	44
Figure 5.6: 20 V <sub>pp</sub> and 50 V <sub>pp</sub> pulses at the outputs of the odd numbered HV drivers measured by 15 pF oscilloscope probe 4 × 11.25° phase difference at 10 MHz. ...	45

Figure 5.7: Frequency step response of PLL changing from the highest (12 MHz) operation frequency to the lowest (8 MHz). A phase margin around 64 degree had been considered in the design procedure. ....	47
Figure 5.8: Output spectrum of PLL when locked at 8 MHz. ....	47
Figure 5.10: Measured phased clock for 4 adjacent channels. The duty cycle is 25%... 48	48
Figure 5.9: Phase noise of PLL locked at 12 MHz. ....	48
Figure 5.11: Radiance sources in non-contact IR thermography from a target. Reproduced from [81]. ....	50
Figure 5.12: IR transmittance of polyethylene film at different wavelengths and different thicknesses. Reproduced and amended from [82]. ....	50
Figure 5.13: The polyethylene oil tank placed on the PCB that holds the wirebonded CMUT array (left), IR camera monitoring the oil temperature while the transducer is driven by the IC (right). ....	51
Figure 5.14: Progressive images of HIFU temperature spot taken in a 11 s. interval: A = 0, B = 4, C = 8, D = 11 s. ....	51
Figure 5.15: Observed HIFU thermal spot when focal point is set at (a) 2 mm, (b) 3 mm, (c) 4 mm, and (d) 5 mm. ....	52
Figure 5.16: Setup for Ex-vivo experiment (left). Thermal lesion on ovine liver after one minute sonication (right). ....	53
Figure 5.17: Designed PCB with 2.5 mm of width for self-heating assessment of HIFU transmitter IC with 350 mW power dissipation. Back and front sides (left). Wire-bonded chip to CMUT array and PCB signal and power pads (center). Two-part epoxy buried device (right). ....	54
Figure 5.18: Thermal assessment of the chip in sunflower oil (left). TMP101 temperature sensor above and below the HIFU transmitter chip. ....	55
Figure 5.19: Eperimental and FEM simulation results of temperature transient at the probe surface while the IC is dissipating 350 mW power. The green line corresponds to the temperature on the heatsink rod of copper. ....	56
Figure 6.1: A possible scheme for reducing the number of cables to be run along the catheter. ....	57

## LIST OF TABLES

Table 1-1: Acoustic properties of different body tissues and organs [14].....	5
Table 3-1: Measured equivalent resistance and capacitance of CMUT array elements. The innermost is 1 and the outer is number 8.....	20
Table 3-2: Thermal parameters used in the simulation.....	24
Table 5-1: Comparisons of the experimental results of the HV driver (single channel).46	
Table 5-2: Thermal parameters used in the simulation.....	55

## LIST OF ABBREVIATIONS

ASIC: Application Specific Integrated Circuit  
CEM<sub>43</sub>: Cumulative Equivalent Minutes at 43 °C  
CMOS: Complementary Metal-Oxide-Semiconductor  
CW: Continuous Wave  
FDA: Food and Drug Administration  
FEM: Finite Element Method  
HIFU: High-Intensity Focused Ultrasound  
HV: High-Voltage  
IR: Infrared  
MR: Magnetic Resonance  
PCB: Printed Circuit Board  
PFD: Phase and Frequency Detector  
PLL: Phase Locked Loop  
PTCA: Percutaneous Transluminal Coronary Angioplasty  
RF: Radio Frequency  
RMS: Root Mean Square  
VCO: Voltage-Controlled Oscillator

# Chapter 1

## Introduction to High-Intensity Focused Ultrasound

Starting fire with magnifying glass by focusing the solar energy onto a small spot is a simple experiment that many of us tried in childhood. In a similar way, focusing of ultrasonic energy with ultrasound transducers elevates the temperature of a spot within a target medium. As an analogy (Fig. 1.1), heat rises only at the focal spot. High-Intensity Focused Ultrasound (HIFU) is a local ablation therapeutic modality for various solid tumors including uterine fibroids, prostate cancer, brain, hepatic, pancreatic, breast and renal tumors as well as neural disorders and atrial fibrillation (AF) [1]. In this technology, the ultrasound beam focused at the target tissue does not harm the propagation medium leaving the surrounding tissue unaffected. Non-invasive (or minimally invasive) nature of HIFU is one of its main advantages over other thermal ablation techniques, which include radio frequency [2], laser [3] and microwave ablation [4]. Although HIFU is generally applied externally (i.e., noninvasively) [1], it can also be applied in a minimally invasive manner through body orifices (such as esophagus, urethra, uterus, and rectum) [5], endoscopically through small incisions [6] or by intravascular means [7].

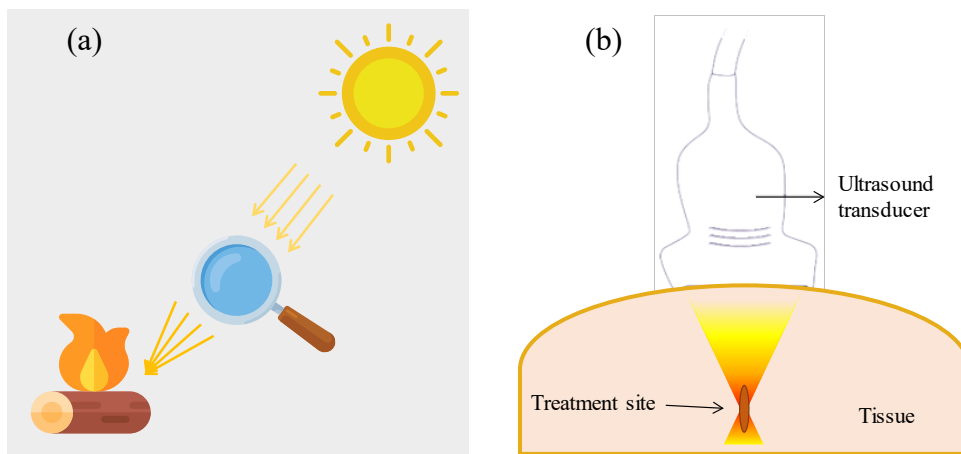


Figure 1.1: Heating a target spot with focused energy: (a) Sunrays, (b) Ultrasound beam.

In the following parts of this chapter the physical principles and medical considerations of HIFU as well as the main components of a HIFU device will be briefly discussed for clarifying the objectives and challenges in this study.

## 1.1 Physical Principles of HIFU

Ultrasound waves generated by a transducer travels through multiple tissue layers, (e.g., skin, fat, muscle), before reaching the target tissue; Within their pathway, they are either transmitted to deeper structures, reflected back to the transducer, scattered or transformed to heat. Loss of energy of ultrasound waves travelling through the body is known as attenuation. The different mechanisms of attenuation include absorption, reflection, diffraction, refraction and transmission [8].

When ultrasound propagates through a tissue layer, the induced pressure fluctuations lead to shearing motion of tissue at a microscopic level, which results in frictional heating. Part of the mechanical energy carried by the incident wave is thus converted into heat by this viscous absorption [9].

At each tissue interface, part of the energy will be reflected, whilst the remaining part is transmitted. The transmission coefficient depends on the difference in acoustic impedance,  $Z_a$ :

$$Z_a = \rho \cdot c \tag{1.1}$$

Where  $\rho$  and  $c$  are density of medium and speed of sound respectively. In the cases there is not considerable difference in acoustic properties, the transmission coefficient is close to unity [10]. Except for fat, air and bone, most tissues in the human body have acoustic properties like those of water. Aqueous media are therefore optimal for transmitting ultrasound energy from the transducer into the body and reflections at tissue interfaces are generally weak, except for the targets like brain which has a strong reflector as skull [9].

Scattering occurs when there are small tissue structures with varying impedances or rough boundaries and dimensions comparable to wavelength on the ultrasound waves direction. Different tissues have different scattering power, with soft tissue and air having the highest, and muscle and bone having the lowest [11]. Refraction occurs when there is a change in direction of sound transmission after hitting an interface of two tissues with different speeds of sound transmission. It is because of change in wavelength to

accommodate the different speed of sound transmission in the differing tissues, which results in a change in direction of the sound wave [8].

The transported energy in an ultrasound wave is characterized by an acoustic intensity,  $I_a$ , measured in  $\text{W}\cdot\text{cm}^{-2}$ , defined as the transmitted energy per unit time and per unit area (usually  $1\text{ cm}^2$ ) in the direction normal to the target area and is relate to the sound pressure,  $p$ .

$$I_a = \frac{p^2}{2Z_a} \quad 1.2$$

Absorption and scattering are two main mechanisms which contribute to ultrasound attenuation. In general, overall ultrasound attenuation is characterized by the following exponential decrease of the pressure amplitude,  $p$ , and of the amplitude of the acoustic intensity,  $I_a$ , with the traveling distance  $z$ .

$$p = p_0 e^{-\alpha z} \quad 1.3$$

$$I_a = I_{a0} e^{-2\alpha z} \quad 1.4$$

Where  $p_0$  and  $I_{a0}$  are the pressure and intensity at  $z = 0$ , respectively. The quantity  $\alpha$  (expressed in  $\text{cm}^{-1}$ ) is the pressure frequency-dependent attenuation coefficient [12]. For most tissues, the attenuation coefficient is related to the ultrasound frequency via a power law of the form:

$$\alpha = a f^b \quad 1.5$$

where  $a$  and  $b$  are tissue-specific constants. In the case of focused ultrasound using spherical transducer the ratio of the beam intensity  $I(0, z_0)$  on axis at focal point  $z = z_0$  to the beam intensity  $I(0)$  at the transducer is:

$$\frac{I(0, z_0)}{I(0)} = \left( \frac{\pi r^2}{z_0 \lambda} \right) = \left( \frac{\pi}{S} \right)^2 \quad 1.6$$

Where  $\lambda$  is the wavelength of the ultrasound wave,  $r$  is the radius of the transducer,  $z_0$  is the radius of curvature and  $S = z_0 \lambda / r^2$ . Thus, if the beam is focused at  $z_0$ , and if  $z_0 < \pi r^2 / \lambda$ , the beam intensity at the geometrical focus will be larger than that at the transducer. This means that the focused transducer will normally be operated with its focal point in a region where the parameter  $S < \pi$ . As shown in Fig. 1.2 the ultrasound wave will be focused to a small cigar-shaped volume whose diameter is  $d_r$  and its length would be around  $d_z$ .

$$d_r = \frac{0.51z_0\lambda}{r} = 1.02\lambda F \quad 1.7$$

$$d_z = 1.22\lambda \left(\frac{z_0}{r}\right)^2 \quad 1.8$$

Where  $F = z_0/2r = z_0/D$  the F number of transducer and D is its diameter. Therefore, while focusing, the effective diameter of lesion can be made smaller by keeping  $z_0 \ll 4r^2/\lambda$  [13].

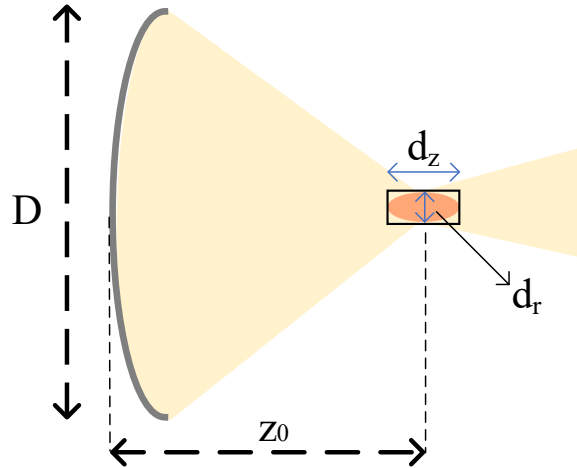


Figure 1.2: Drawing of spherically curved transducer and its focusing cigar-shaped beam pattern with diameter of  $d_r$  and length of  $d_z$ .

Unlike other ablation methods, such as radio-frequency, laser or microwaves, the attenuation of sound through aqueous media at ultrasound frequencies is sufficiently low that adequate levels of energy required during the treatment can be delivered to the target tissue. The optimal choice of therapeutic ultrasound frequency is application-specific and represents a compromise between treatment depth and the desired rate of heating. Frequencies near 1 MHz have been found to be most useful for heat deposition, with frequencies as low as 0.5 MHz being used for deep treatments and as high as 8-12 MHz for shallower treatments [10]. Table 1-1 summarizes acoustic properties of biomedical media.

Table 1-1: Acoustic properties of different body tissues and organs [14].

Tissue type	Wave speed (m/s)	Acoustic impedance (MRayl)	Attenuation (dB/cm/MHz)
Blood	1550	1.67	0.15-0.25
Liver	1578	1.66	0.4-1
Fat	1430-1450	1.33	1
Muscle	1585	1.7	0.57-3
Brain	1540-1550	1.68	0.44
Bone	3200-4000	6.47	30
Air	333	$430 \times 10^{-6}$	

## 1.2 Medical Considerations of HIFU

Rising the tissue temperature to 55 °C and maintaining that for a few seconds will lead to coagulative necrosis and immediate cell death [15], [16]. Cumulative Equivalent Minutes at 43 °C ( $CEM_{43}$ ) suggested by Dewey and Sapareto [15] is a thermal dose parameter by which any time-temperature therapy history is converted to the required minutes at 43 °C and is given by:

$$CEM_{43} = R^{(43-T)} \Delta t \quad 1.9$$

where R is 0.5 and 0.25 for temperatures above and below 43 °C, respectively, and  $\Delta t$  is the exposure duration. As an example, 20 °C temperature rise from 37 °C body temperature yields a  $CEM_{43}$  value of 273 minutes. This means that, heating the tissue for 1 second at 57 °C will be equal to 273 minutes heating at 43 °C. The largest reported  $CEM_{43}$  threshold for thermal damage in human tissue is 600 minutes for the skin, while this value is 240 minutes for liver, kidney and muscle and 10 minutes for brain [16], [17].

Based on continuous wave (CW) or pulsed excitation mode of transducer, HIFU interact with biological tissues in “heat-induced” or “acoustic cavitation” ways. While CW HIFU showed high damaging effect due to thermal ablation, it seems the pulsed mode HIFU is effective in increasing the efficacy of a variety of drug therapies. Generally, it is presumed that the most damaging effects in pulsed HIFU treatment are cavitation and mechanical effects and it acts to temporarily increase the permeability of the tissue to better deliver the therapeutic agent [9], [18].

### 1.3 Main Components of HIFU System

Ultrasound transducer and its driving system are the main parts of a HIFU system, however, different driving architecture may be employed based on the type and geometry of the transducers. As showed in the Fig. 1.3, spherically-curved transducer, flat transducer with interchangeable lens and phased-array transducers can provide beam focusing for HIFU application. While single element transducers need only one amplifier (or pulser) for driving, the phased-array transducers should be driven by an array of the same amplifier and a phase shifter. In addition, according to the depth of target tissue energy-delivery routes, the HIFU devices are divided into transrectal or intravascular (minimally invasive) and extracorporeal

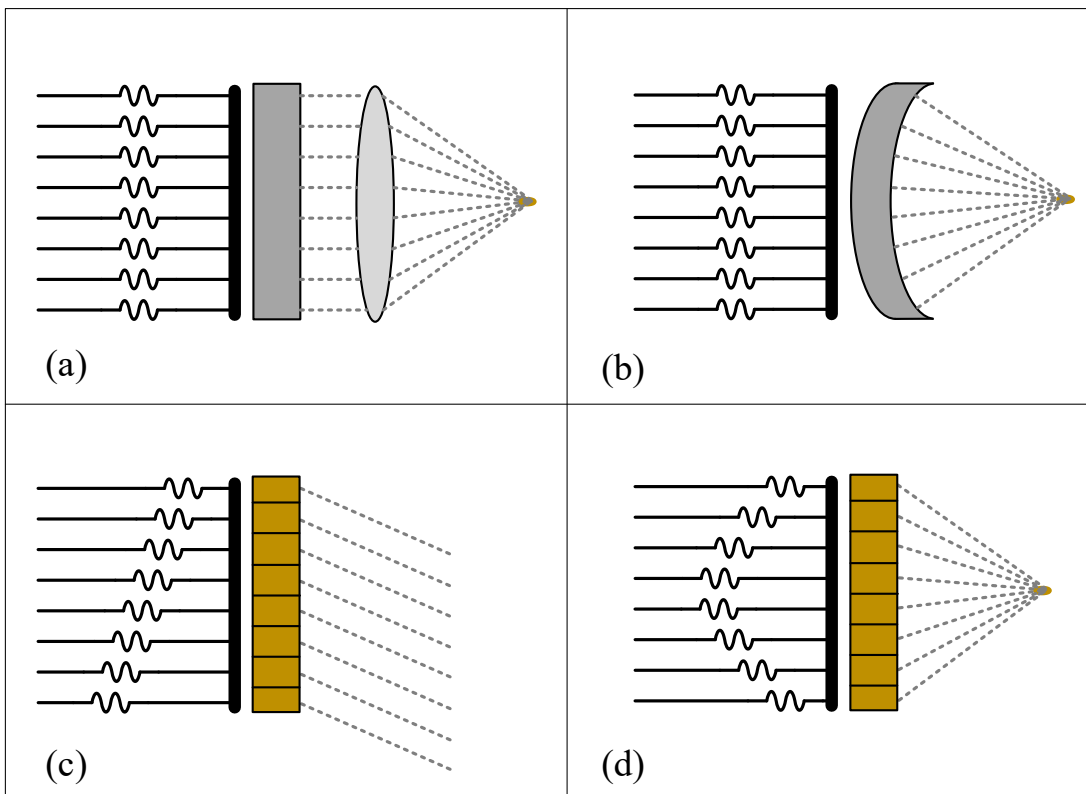


Figure 1.3: Different methods of ultrasound wave focusing: a) Flat transducer and interchangeable lens, b) Curved transducer with constant focal point, c) Phased-array transducer without focusing, d) Phased-array transducer with adjustable focusing.

(non-invasive) types as also mentioned earlier. Therefore, for very compact HIFU devices and for eliminating the non-idealities and losses in the cable connections, an array of integrated drivers on a chip close to the transducer would be essential.

The driving circuitry has to transfer considerable amount of AC power to the transducer at relatively high voltage (50-300 V) in MHz range. In addition, in the phased-array devices, based on CW or pulsed mode of HIFU operation, the high-voltage (HV) driver array should be capable of generating phase shifted or time delayed signals/pulses via a signal generator. Ensuring that the HV driver is efficient enough is very important since it is the most power consuming block of the system and any dissipated power will result in self-heating.

In order to monitor the operation progress during the HIFU therapy, image guidance from the tissue is necessary. These images may be either provided by ultrasound or MR (magnetic resonance), hence the HIFU devices are also classified into ultrasound- and MR-guided. Ultrasound imaging guided devices are relatively economical, real-time and can provide HIFU beam propagation precisely since the imaging and therapeutic ultrasound waves share the same pathway. Moreover, the integration of imaging and therapeutic units on a single device can be achieved in ultrasound imaging guided devices. On the other hand, MR imaging modality provides excellent contrast and is not limited field of view. MR can quantify changes in temperature and thermal dose of the treated tissue directly [19].

## 1.4 Research Objectives

While external HIFU probes typically have quite large acoustic apertures, operate at relatively low frequencies ( $\sim 1$  MHz) and deliver large acoustic powers to its target, HIFU probes used in minimally invasive procedures have to be built ergonomically and small in size to be considered as part of the surgical tool set [6]. These small HIFU probes compensate their loss in acoustic aperture by getting close to the target and by using higher ultrasound frequencies ( $\sim 10$  MHz) [20]. Such HIFU probes would be especially effective for small and hard to reach targets. A special case for such an application would be the brain. Because the skull is a strong acoustic reflector and absorber, getting enough acoustic field intensity to the focal point, and confining it to the target are major issues [21]. There are two workarounds to this issue: endoscopic treatment through a burr hole in the skull opened by trephination or reaching the target spot by intravascular means. Both cases would require a small HIFU probe with minimal cable count to improve its ergonomics.

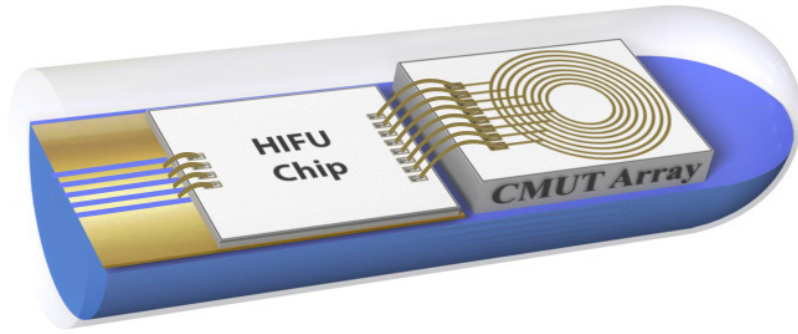


Figure 1.4: Conceptual drawing of HIFU Catheter Ablation System. The radial distance of the ablation spot will be set by the phase of the individual drive pulses applied to the elements of the ring array

In this study, we proposed, designed, manufactured and tested a CMUT-based intravascular HIFU catheter with an integrated driver IC. The transducer array and driver IC can be fitted onto a 6-Fr catheter probe as depicted in Fig. 1.4. The concentric ring array of 2 mm diameter used in the probe was fabricated in the Nanotechnology Research and Application Center (SUNUM) of Sabanci University Fig. 1.5.

The transducer drive signals could have been externally generated and carried in coaxial cables along the catheter. Though simpler, this method requires a high number of micro-coax cables to be placed along the catheter, which is costly, and greatly impacts the electrical performance of the wire bundle carrying high-voltage phased signals to the transducer [22]. A typical 2-meter coaxial cable has a capacitance of 200 pF [23], which is one order of magnitude larger than the 11-13 pF capacitance of each array element, resulting in poor drive efficiency. The proposed solution to these issues is the local generation of the signals, which reduces the wiring requirement to power cables and a data line. In addition to reducing the number of cables, putting a HIFU drive front-end IC close to transducer array within the catheter improves signal integrity and drive efficiency. There are similar studies on the integration of the front-end electronics with the transducer array [24], [25], [26] in ultrasound imaging. In all such applications, the common concern is the limitation on dissipated power by the front-end IC inside the

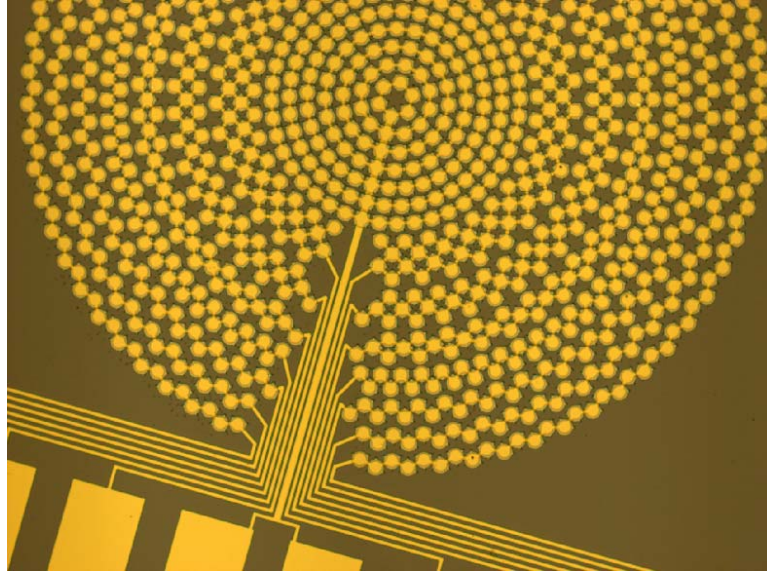


Figure 1.5: Microscope image of the 8-element concentric array used for the catheter ablation system. Each of the 8 elements of the array have equal area. Cell diameter is  $44\ \mu\text{m}$ . The device was fabricated on a highly conducting Si substrate using surface micromachining techniques. While the membrane material is PECVD  $\text{Si}_3\text{N}_4$ , Au/Cr is used as the electrode material.

catheter. The surface temperature on the probe should be limited by  $42\ ^\circ\text{C}$ , the endurance limit of human tissue [27], [28]. This is a more profound issue in HIFU as the front-end IC will run in CW mode for a prolonged duration to reach the therapeutic HIFU dose. Consequently, a thorough thermal analysis is required.

In order that the final device can be considered for different target tissues with adjustable spot size and penetration depth, a HV driver IC with variable operation frequency is desired to design. In addition, while delivering adequate thermal dose at the focal point to the medium, surface of the device must not exceed the safe operation temperature due to self-heating. Conceptual drawing of proposed HIFU catheter ablation system is shown in Fig. 1.5. Based on the design parameter and characterization data of the CMUT device, the HV driver IC will be designed accordingly.

## 1.5 Organization of Dissertation

Parts of this thesis were originally published in “*IEEE Transactions on Biomedical Circuits and Systems*” as (Integrated HIFU Drive System on a Chip for CMUT-Based Catheter Ablation System) in [29] and are reproduced in here. This chapter was a short review on physic of focused ultrasound and principle of ultrasound wave transmission

into a target tissue. We also had a brief introduction to medical requirements thermal ablation therapy. By introducing main blocks of a HIFU system, the target of this research was discussed.

In the next chapter we will review HIFU systems that are either officially approved or under clinical test or subject of ongoing research. In the third chapter system design steps of the proposed HIFU device is presented in detail. It includes design considerations for each block of HIFU transmitter IC besides the system level requirement of device for safe operation during the treatment. We will see that one of the most challenging part of this study is to overcome the self-heating concerns of integrated transmitter chip.

The forth chapter provides the details of circuit design steps for all block of the designed two HIFU transmitter ICs. As will be discussed later, in this study an 8-element HV buffer combined with different transmit beamforming circuitries (digital and analog) were designed as two separate chips. In the digital pulse generator, a 128-192 MHz reference clock generator along with an array of 4-bit counters generate the 8-12 MHz phased trigger signals for the HV buffer array. But in the analog pulse generator, the trigger signals are generated from the phased clock references which are directly produced by an 8-12 MHz Phase Locked Loop (PLL).

Measurement results of the chip for each block along with system-level characterizations are discussed the fifth chapter. The heating capability of the HIFU system is visualized in real-time by infrared thermography. Also, to verify the thermal dose delivering capability of the device, Ex-vivo experiment has been performed on ovine liver. In the last section of this chapter, self-heating of the probe surface is investigated experimentally and compared with FEM simulations. Chapter six concludes the thesis with future work suggestions for further improving the fully integrated HIFU catheter system.

## Chapter 2

### Overview of HIFU Systems

#### 2.1 Existing HIFU systems

Many multi-element Phased-array HIFU systems are currently being used clinically as FDA-approved devices for either transrectal or extracorporeal treatments. Echopulse<sup>®</sup> is another HIFU device with integrated imaging for breast cancer treatment. This device includes an ultrasonic transducer, an amplifier, a computer, visualization and treatment unit as well as an interchangeable cooling system [30]. Sonablate<sup>®</sup> is a minimally invasive robotic HIFU device for treating prostate cancer with real-time ultrasound imaging capability compatible with MRI [31]. Ablatherm<sup>®</sup> Robotic is also a non-invasive treatment for prostate cancer with integrated imaging. This device has two different transducers, one operating at 7.5 MHz for imaging and other one at 3 MHz for therapy [32]. Sonatherm<sup>®</sup> is a robotic laparoscopic probe used to deliver precise and focused

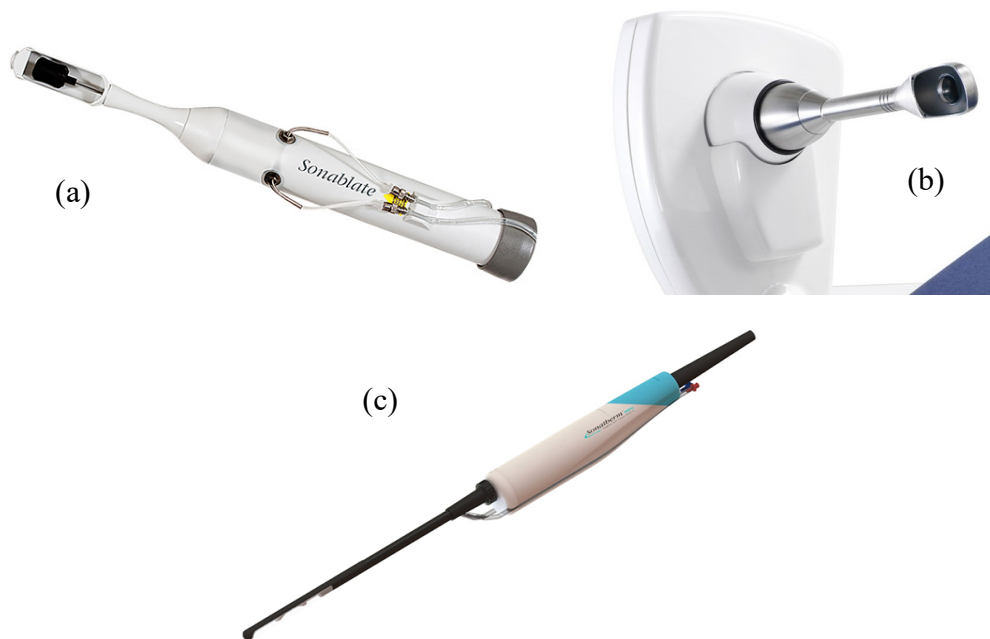


Figure 2.1: Some of commercial HIFU systems: (a) Sonablate<sup>®</sup>, (b) Ablatherm<sup>®</sup>, (c) Sonatherm<sup>®</sup>

ablative energy to soft tissue with a customizable zone of ablation. With a 4 MHz HIFU transducer and a 6.5 MHz ultrasound imaging transducer has a 35 mm focal length. The probe has 11 mm tip diameter and uses a water cooling system to keep its temperature in the safe region during the surgery [33].

## 2.2 Catheter-based HIFU devices

More advanced type of HIFU systems are the catheter-based devices which can be positioned directly within or adjacent to the target and coagulate it precisely. These devices may require shorter heating time providing better energy localization. Catheter-based HIFU devices include interstitial applicators directly placed within the target volume, endoluminal devices placed within lumen or body cavities and endovascular or cardiac applicators placed through or within major blood vessels [34]. As an example, is the transurethral device developed by Phillips that whose original prototype was from academic area [35]. This device includes a therapy control workstation using clinical software, a radiofrequency generator, a rigid, water-cooled transurethral US applicator (5 mm [15 F] diameter) with eight transducer elements (4×5 mm/element), a motor unit enabling rotation of the applicator, and a standard clinical MRI scanner (Achieva 3.0T, Philips Healthcare, Best, the Netherlands).

A 7-sided interstitial device reported in [36] for brain ablation is developed by Carthera. The device comprises 56 planar piezocomposite ultrasound elements operating at 6 MHz, oriented on the seven faces of a 3.2 mm flexible catheter. This device is also originated from a university domain work in Labtau at Inserm. Another catheter-based device is a dual-mode ultrasound arrays for percutaneous and laparoscopic applications developed by Guided Therapy Systems which is a 32-element arrays with aperture 2.3×49 mm and therapy frequency at 3.1 MHz [37].

Another HIFU catheter developed by Johnson & Johnson operating at 8 MHz [38] to treat atrial fibrillation by ablating tissue surrounding the pulmonary vein. The body of the catheter is 8-F and it can accommodate a 0.035-inch guidewire in a central lumen.

A bi-directional endocervical HIFU catheter with sectored tubular transducers integrated within a tandem holder was used in [39] for treatment of locally advanced cervical carcinoma. This device includes three tubular transducers of 3.5 mm in diameter, 10 mm

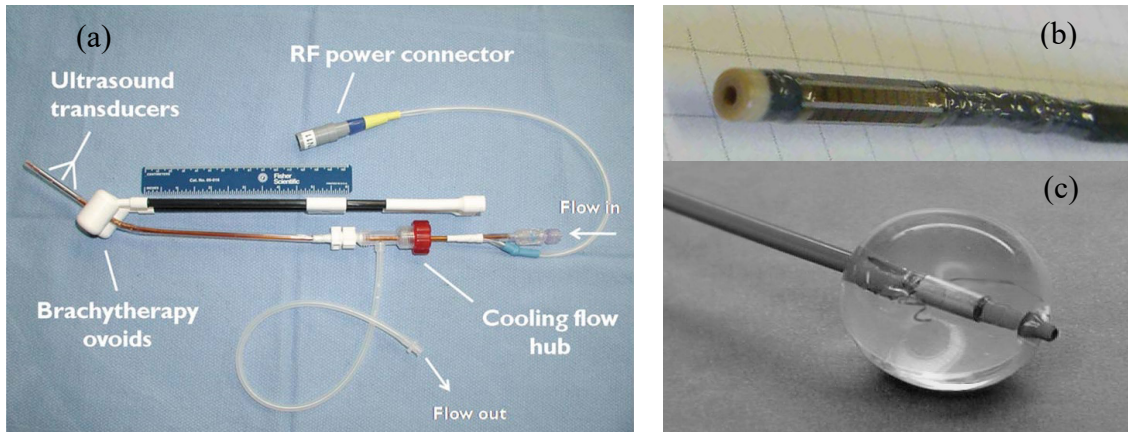


Figure 2.2: Some of available catheter-based HIFU devices: (a) A bi-directional endocervical HIFU catheter for treatment of locally advanced cervical carcinoma [39]. (b) 7-sided interstitial device for brain ablation by Carthera [36]. (c) Transballoon HIFU catheter developed by Johnson & Johnson for atrial fibrillation treatment [38].

in length operating within a 6.5–8 MHz range. Transducer sectors are individually wired with coaxial cable connected to Redel RF power connectors (Lemo S.A.) at the back end. The transducer assembly is covered with a thin layer of epoxy (310M, Epoxy Technology) and polyester heat shrink (4.8 mm OD, Advanced Polymers). An outer polyimide tubing layer (3.4 mm OD, Professional Plastics) protects the cables and provides structure.

In all above summarized devices, transducers are of piezoelectric type and their main concern is the cooling of the transducer surface. Thermal conductivity of pzt is  $\sim 1.5 \text{ W/(m.k)}$  and the driving loss will heat up the device quickly. In the next section we investigate the ongoing research and available prototypes which utilizing capacitive transducers.

## 2.3 CMUT based HIFU catheters

Two main types of ultrasound transducers include piezoelectric and capacitive. Capacitive Micromachined Ultrasound Transducers (CMUTs) have shown important advantages over traditionally used piezoelectric transducers that make them more attractive for use in catheter ablation devices: CMUTs do not need backing and matching layers which makes them relatively smaller in thickness and easier to manufacture [40]. Moreover, the CMUT suffers less from self-heating because of the higher heat conductivity of silicon which is the conventional substrate material [41], [42]. Additionally, as CMUTs are manufactured using lithographic techniques, the complexity

of the array structure does not hinder the process. As discussed earlier, array of transducer elements is being used in the HIFU devices for better controlling the ablation point, therefore CMUT seems to be the best candidate to this end. In addition, one of the main considerations in catheter-based HIFU systems is electrical to acoustic conversion efficiency by the transducer. CMUTs show very good efficiency [43], especially with novel fabrication techniques for parasitics reduction [44], comparing with the conventional piezoelectric transducers.

By the recent advent of CMUT, this type of transducer is attracting increasing interests but CMUT-based HIFU systems are still either under clinical tests or currently under development at academic research institutions. In [45] by expressing the advantages of CMUT over piezo-based transducers, presented a CMUT-based catheter and claimed (HIFU) ablation of the prostate can be done through the wall of the urethra using a transurethral instead of conventional devices through the rectal wall with a transrectal probe. The transurethral approach has several safety-related advantages as compared to the transrectal approach. Because the location of the urethra is known (probe within urethra), it is easier to avoid unintentional thermal damage to the urethra that might increase the risk of incontinency. Moreover, since there is no sonication through the rectal wall, the risk of damaging this sensitive structure is also significantly reduced. It also noted that the main disadvantage of the transurethral approach is that the space available for the transducer is substantially reduced as compared to the transrectal approach. This means that small-diameter probes are useful in the case of prostate diseases or in treating any hard-accessible tissues like puncture hole (for ablation of liver).

In [46] three interstitial CMUT prototypes were fabricated for the final catheter prototype of ten facets and six independent couple of elements per facet. The CMUT-based high-intensity contact ultrasound (HICU) catheter incorporates ten 1-D linear arrays, 32.4 mm long and 0.8 mm wide (12 elements, electrically coupled 2 by 2, per face). The arrays are mounted on a cylindrical 9-French flexible catheter, which formed a prism-shaped 2-D array for multidirectional radial ultrasound exposures. The device was driven by external amplifier at 6-8 MHz and could elevate the temperature more than 20 °C over the target radii more than 15 mm. This prototype is a new version of the above mentioned 7-sided piezoelectric-based catheter reported in [36].



Figure 2.3: CMUT-based ten facets HICU catheter prototype [46].

Lately in 2017 Prof. Khuri-Yakub's group presented in IEEE International Ultrasonics Symposium (IUS) a new CMUT-based dual mode catheter with  $32 \times 32$ -element 2-D CMUT array for ultrasound image guidance and HIFU ablation with integrated ASIC. The device generates the maximum pressure at the focus with 60-V AC and 95-V DC around 13 MPa peak-to-peak but there is now detail about the power consumption and self-heating issues when in HIFU operation mode that is the main concern in such device [47].

In almost all above mentioned devices, the high-voltage driving circuitries are outside of the probe and connected to the transducer array via long cables. While self-heating of transducers in piezoelectric-based HIFU systems is one of the most crucial parameters, thanks to high thermal conductivity of silicon (148 W/(m.k)), CMUT-based devices have safer transducer surface. But here for our proposed fully integrated HIFU catheter system the self-heating concern arises from the power dissipation of transmitter IC. In such case, an application specific integrated circuit (ASIC) should be designed and connected to the transducer in the small area on the tip of catheter while carefully considering all heating issues of chip. As the silicon substrate of the chip has high thermal conductivity, by designing an appropriate heatsink structure attached to the chip the generated heat may be distributed to a larger area which leading to a considerable temperature drop on the area above the chip.

This study can also pave the way for development of fully integrated imaging and HIFU catheters with very compact systems which don't need to MRI guidance and cooling systems. Considering the increasing interest for ultrasound imaging-guide HIFU therapies as one of the safest and most accurate therapy methods, it is highly promising to integrate the electronic part with the transducer within a probe to considerably reduce the data cables. Since a dual mode catheter can operate in only one mode, imaging or HIFU therapy, in a moment and knowing that the devices consumes higher power in

HIFU mode, fulfilling the temperature safety of the system against power dissipation would guarantee the safety of the device in both modes.

## Chapter 3

### Design of Integrated HIFU Catheter System

HIFU, as implied by the name, relies on the focusing gain of an ultrasound source, and aims the generation of a relatively strong field spot to coagulate or mechanically destroy cells at the target, while inducing no harm to the surrounding tissue. For a particular application, target tissue, spot size, and penetration depth dictate the transducer properties and operation frequency, due to the dependence of acoustic attenuation to the tissue type and excitation frequency [48]. In this chapter, we will firstly investigate the physical requirements and of a HIFU system integrated on a catheter, based on the acoustic properties of the target tissue and our interested HIFU beam pattern and penetration depth; Following by that, ANSYS simulation results to define the power budget of the chip and the safe operation duration of the system have been reported.

#### 3.1 Block-level Specifications

In the application that is the subject of this study, the aim is to design a HIFU system suitable for intravascular use. This limits the size of the transducer and its driver IC by the vessel diameter. Considering the size of a typical PTCA catheter of 6 Fr, the transducer diameter was chosen as 2 mm. This sets the operation frequency to 8-12 MHz to maximize the focusing gain within the useful focal depth of the transducer, when human muscle is the target tissue [49], [50]. For obtaining the best efficiency, the number of phased elements is chosen as 8 to achieve a normalized peak pressure of 95% with respect to a transducer with infinite phase resolution [51]. The natural focus of a piston transducer (or the ring array driven with no phase difference between elements) is at  $z_0 = D^2/4\lambda$ , where  $D$  is the diameter, and  $\lambda$  is the acoustic wavelength in the propagation medium [13]. This value, which is found as 6.7 mm at 10 MHz for the transducer to be used in the proposed system, determines the useful penetration depth of the HIFU spot. The size of the spot at this focal point, on the other hand, is  $D/2$  in width, and  $4.88\lambda F^2$  in

depth (Eq. 1.8), where  $F$ , is the f-number of the transducer given by  $F = z_0/D$ . Substituting  $z_0 = 4$  mm, the approximate spot size is determined as  $1 \text{ mm} \times 3 \text{ mm}$ .

In this study, two ICs were totally implemented with the same HV driver array but different phased-array trigger pulse generation topologies. For this reason, the pulse generators will be discussed as “digital pulse generator” for the first chip and “analog pulse generator” for the second chip while HV driver blocks are common in both.

### 3.1.1 Digital Pulse Generator and Phase Locked Loop

Fig. 3.1 shows a block diagram of the HIFU system, which comprises an 8-element concentric CMUT ring array, and a HIFU transmitter IC, with a PLL as reference clock generator, digital pulse generator, and CW high-voltage buffers. The drive signals for each individual array element are generated by the digital pulse generator section of the IC, each channel of which divides a clock signal of larger frequency. A division rate of 16 provides a phase accuracy of  $11.25^\circ$  which is reasonable for an 8-element array. Consequently, the tuning range of the high frequency clock source should span the interval 128-192 MHz for the generation of drive signals in the interval 8-12 MHz.

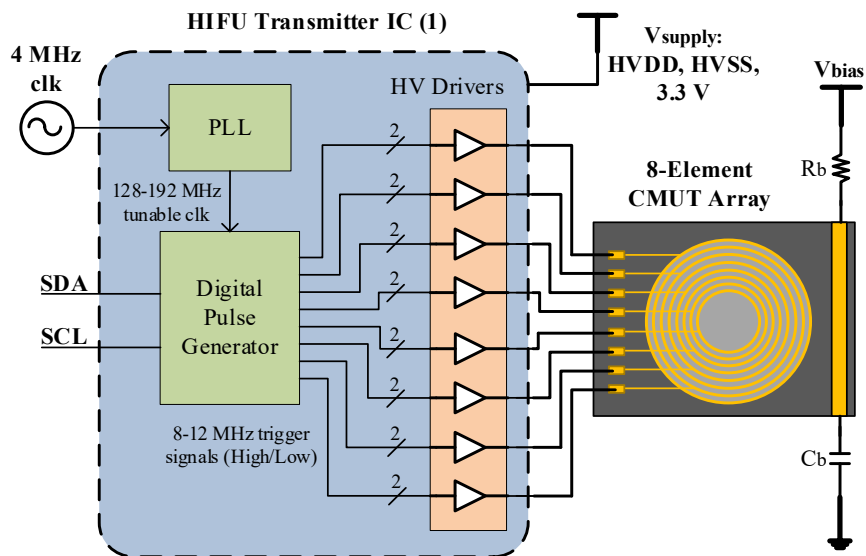


Figure 3.1: Block diagram of HIFU system with the first chip. All functional blocks of a complete array driver, which include a PLL with an integrated VCO, a digital pulse generator, and HV drivers are combined on a single chip.

The source for the high frequency clock is a phase locked loop (PLL) with an integrated voltage-controlled oscillator (VCO). Owing to the relatively wide tuning range (40%), and low operation frequency, a ring VCO was preferred. Compared to an LC

oscillator, a ring VCO consumes less power, and occupies less chip area at the price of increased phase noise. Additionally, removal of an inductor makes the system MR-compatible.

### 3.1.2 Analog Pulse Generator

The digital phase shifter based on programmable counter used in the first chip needs a reference clock signal at high frequency. In the second chip, by combining the PLL and pulse generator blocks the required phased shifts were obtained from a low-frequency PLL frequency synthesizer. For this purpose, an eight-stage differential ring VCO generates 16 different phases. The PLL is tunable between 8-12 MHz with 16 steps of 250 KHz. Using two 16×1 multiplexers for each channel any of the generated phases can be transferred to the HV drivers. The PLL operates in the same frequency of HV drivers and while consuming lower power and occupying smaller area with respect to the first chip. Block diagram of the HIFU system with the second chip is shown in the Fig. 3.2.

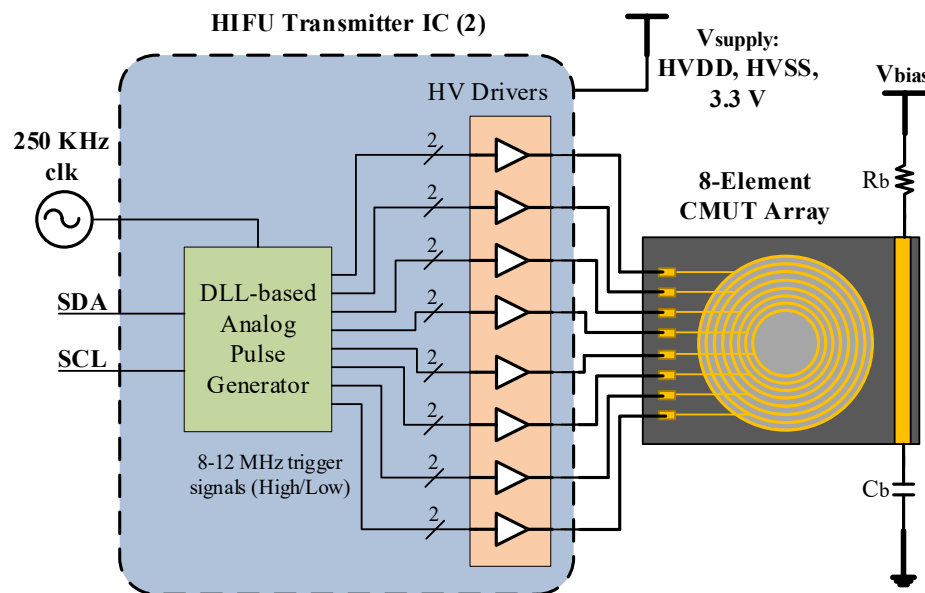


Figure 3.2: Block diagram of HIFU system with the second chip. The trigger pulse generator integrated in an 8-12 MHz PLL.

### 3.1.3 Continuous-Wave Eight-Channel High-Voltage Driver Requirements based on Characterization of CMUT Arrays

One primary design specification for a catheter-based system is to limit the surface temperature. This requires design of an efficient driver section to limit circuit self-heating, taking into account that the circuit will operate in CW mode, as opposed to an imaging

system which generates momentary pulses. The design of the driver section requires the knowledge of the nature and the associated component values for the load. Equivalent electrical impedance of a CMUT can be represented as the parallel combination of  $C_P$ , the parallel-plate capacitance between the CMUT membrane and the common node, and a resistor ( $R_P$ ), the medium's mechanical load at the CMUT surface, transformed to the electrical port [52]. To measure the impedances of a CMUT array, a sample device was wire-bonded to an FR4 PCB and by using an Agilent 4294A Impedance Analyzer  $C_P$  and  $R_P$  were extracted (Fig. 3.3). The values of these components for the transducer used in the system are listed in Table 3-1, which were measured by while the device was immersed in sunflower oil, and the DC bias was set to 130 Volts.

Table 3-1: Measured equivalent resistance and capacitance of CMUT array elements. The innermost is 1 and the outer is number 8.

Element Number	10 MHz		12 MHz	
	$C_P$ (pF)	$R_P$ (k $\Omega$ )	$C_P$ (pF)	$R_P$ (k $\Omega$ )
1	12.6	13.5	12.6	9.8
2	12.4	13.2	12.4	9.7
3	12.2	12.8	12.2	9.5
4	12.7	11.4	12.7	7.9
5	12.5	10.7	12.5	7.3
6	13.4	10.0	13.4	7.1
7	13.0	9.00	13.0	6.5
8	11.1	7.20	11.0	5.5

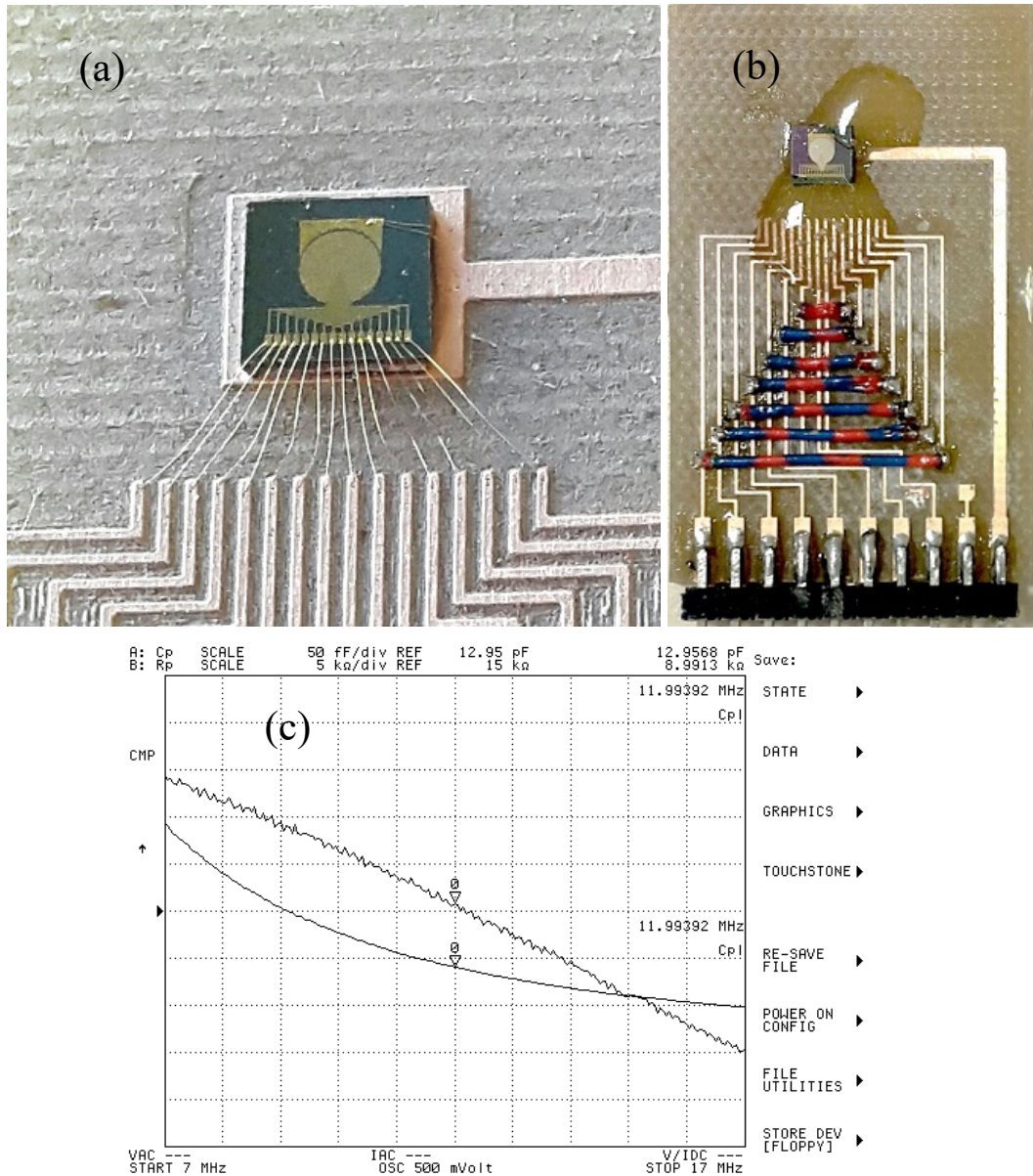


Figure 3.3: Impedance measurement of a CMUT element: (a) Wire-bonded device to PCB, (b) coated with two-part epoxy for protection of wires, (c) measured impedance of one element when the device is immersed in oil.

The transferred power to the resistive part will be the useful power converted to acoustic pressure (heat) at focal point and the consumed power for charge and discharge of capacitive part will be counted as unwanted dissipated power. Although smaller  $R_P$  values are desired for greater driving efficiency [53],  $C_P$  dominates, and the load is primarily capacitive. Most of HIFU systems in literature have used external HV power amplifiers/pulsers for driving the ultrasound transducers due to power requirements [5], [54], [55], [56], [57]. The HV linear amplifier, which is the most commonly used circuit for driving piezoelectric transducers [58], suffers from low power efficiency, and

therefore is not suitable for this design. In order to increase the efficiency of HV drivers, tuning out the load capacitor  $C_P$  [59], or decreasing unwanted harmonics by using a pulse-shaping driver [53] are suggested; but these methods need off-chip components for each channel, which are not acceptable for our application, due to area and MR compatibility concerns. For this chip, a HV pulser with large push-pull transistors at the output stage is considered. The HV driver circuit for this chip should have small footprint while being capable of driving a load of at least 13 pF with 20 V<sub>PP</sub> pulses at 12 MHz. In order to make the driver capable of handling larger transducers as well, the design of HV driver was aimed for 20 pF load, while the target pulse amplitude is increasable to the upper limit of the IC technology (which is 50 Volts) so that larger acoustic output can be produced, when necessary.

Although the proposed system would not be portable, power limitation arises from heat dissipation considerations for a tightly packaged integrated probe. Dissipated power of a push-pull driver circuit with capacitive load can be estimated by:

$$P = C_P V^2 f \quad 3.1$$

where  $f$  is the switching frequency and  $V$  is the pulse magnitude. Although In the literature [60], 5 W power dissipation has been mentioned to be tolerable for therapeutic probes, the power budget will be defined based on the ANSYS simulation or worst case without considering convection cooling effect of blood flow. For a drive voltage of 20 V<sub>PP</sub> at 12 MHz into a 12.5 pF load, the power dissipation is estimated as 60 mW for a single channel, which adds up to 480 mW for the entire driver section. These estimations form the basis for the analysis regarding the thermal performance of the proposed system.

## 3.2 Safe Operating Region for The Integrated HIFU Catheter

To assess the temperature of catheter surface as a function of the HV supply level, we ran a simulation in ANSYS Multiphysics (ANSYS, Inc., Canonsburg, PA 15317) to find the appropriate HV supply level and define the safe operation conditions for catheter inside the body. The axisymmetric model of Fig. 3.4 was constructed using PLANE13 2D coupled field solid with temperature degree of freedom, and has a radius of 5 mm and height of 10 mm. A 500  $\mu$ m radius silver rod of height 5 mm is assumed to be placed into an epoxy coated catheter with 2 mm diameter.

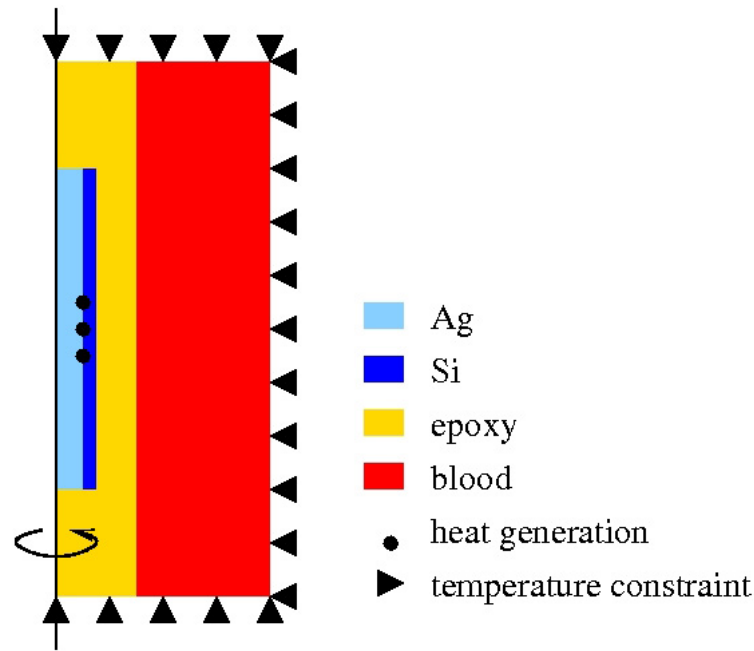


Figure 3.4: FEM model of catheter tip used in thermal simulations. The axisymmetric model assumes that the IC is placed on a silver block and encapsulated in a low thermal conductivity epoxy layer. The entire model is stationary; cooling effect of blood flow is not included.

The catheter is assumed to be placed in a blood-filled vessel. The chip is modeled by a 200  $\mu\text{m}$  thick silicon layer wrapped around the silver rod, extending through a 2 mm section. This is a reasonable assumption as most of the heat will be absorbed by the silver rod due to its significantly large thermal conductivity. The outer surface of the model is assigned a temperature constraint of 37  $^{\circ}\text{C}$ . We run simulations for various power levels, which are applied as heat generation force loads to the silicon wafer section of the model. After a number of trials, we found that 500 mW of heat generation results in a temperature rise to about 42  $^{\circ}\text{C}$  in 100 seconds. The result of the transient analysis is shown in Fig. 3.5 This power level corresponds to a drive voltage of 20  $V_{\text{PP}}$  at 12 MHz for a total CMUT device capacitance of 100 pF. In reality, however, we expect that blood flow in the vessel will improve the situation by providing additional convection cooling which is not considered in this simulation. lists the material parameters used in the simulations.

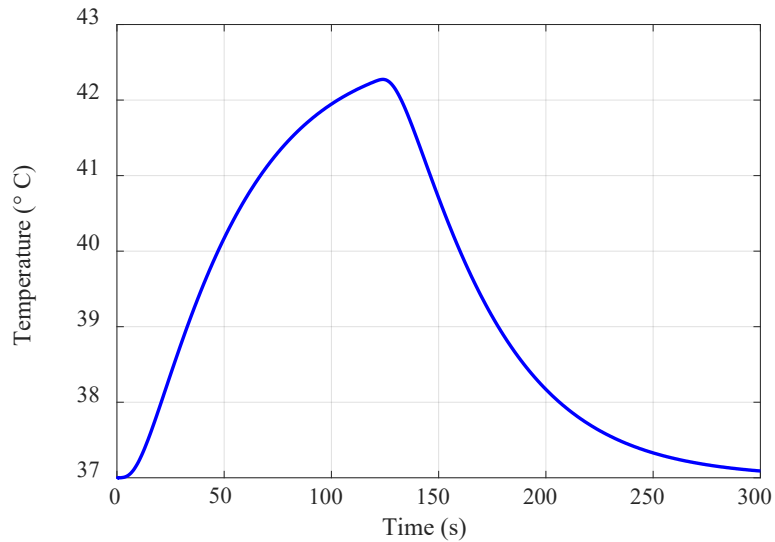


Figure 3.5: FEM simulation result of temperature transient at the catheter surface while the IC is dissipating 500 mW of power. The temperature exceeds safety limits after 100 seconds.

Table 3-2: Thermal parameters used in the simulation

Material	Thermal Conductivity (W/mK)	Specific Heat (Joule/kg °C)	Mass Density (kg/m <sup>3</sup> )
Ag	406	240	10490
Si	149	705	2329
Human Blood	0.520	5617	1035
Polyurethane	0.020	1800	2000

The next step in simulations was an assessment of the tissue heating performance of the proposed system with the calculated drive voltage level. CMUT output pressure data is obtained by running a transient simulation for a CMUT whose parameters have been found by matching the electrical impedance data of the device in Fig. 1.4 (membrane thickness 2  $\mu\text{m}$ , gap 170 nm,  $\text{Si}_3\text{N}_4$  isolation 200 nm, Young's modulus 105 GPa, Poisson's ratio 0.27, mass density 2330  $\text{kg/m}^3$ ). The model, which contains a single CMUT cell, is constructed using SOLID45 and TRANS126 elements, and was loaded with a water column modeled with FLUID30 elements. The water column was constrained from movement in lateral directions so that the device behaves as if in an infinite field of CMUTs. A transient simulation for 20  $V_{\text{PP}}$  pulses at 10 MHz at a bias

voltage of 130 V shows that the RMS pressure at 96  $\mu\text{m}$  distance from the surface of the CMUT device is 395 kPa (Fig. 3.6).

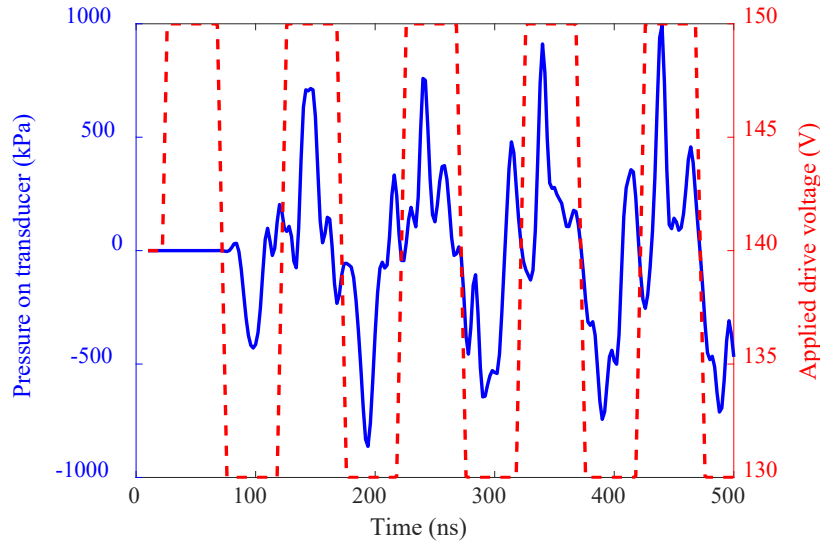


Figure 3.6: FEM simulation result showing the generated pressure at 96  $\mu\text{m}$  distance from the surface of the CMUT used in the HIFU system. The transducer is biased at 130 Volts DC and driven with 20 Vpp amplitude at 10 MHz. The RMS pressure is 395 kPa.

This approach is assumed as a full model of the entire array is infeasible to construct. The surface pressure data is fed into a simulation based on plane wave decomposition to compute the acoustic field distribution by the 8-element CMUT array in the propagation medium, which was assumed to be sunflower oil. The acoustic attenuation  $\alpha$  was taken as  $52.8 \text{ NP m}^{-1}$  at 10 MHz [61]. The focal distance is set as 4 mm. The field data is then used as heat generation in another axisymmetric model in ANSYS. Thermal conductivity, heat capacity and mass density of sunflower oil was taken as  $0.168 \text{ W/mK}$ ,  $2250 \text{ J/kgK}$  [62] and  $920 \text{ kg/m}^3$ , respectively. The analysis shows that the temperature at the focal point rises from  $37 \text{ }^\circ\text{C}$  to around  $56 \text{ }^\circ\text{C}$  in 11 seconds as shown in Fig. 3.7.

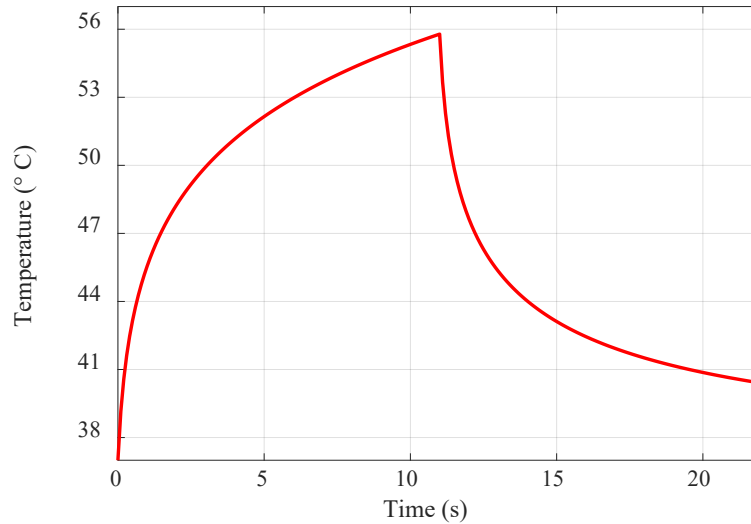


Figure 3.7: Simulation result of temperature generated by the CMUT ring array at a focal distance of 4 mm. A temperature rise of 19 °C is anticipated in 11 seconds.

According to Eq. 1.9 the FEM result of 19 °C temperature rise yields a CEM<sub>43</sub> value of 136.5 minutes. This means that, heating the tissue for 1 second at 56 °C will be equal to 136.5 minutes heating at 43 °C. As an example, for the largest reported CEM<sub>43</sub> requirement in human tissue is 600 for human skin. The total exposure time required to reach this value (including the 11 seconds rise time) is 15 seconds, for which the catheter temperature is expected to reach just 38 °C which does not violate the 42 °C limit. For stronger exposure requirements, water cooling microsystems [22], [27], [54] may be employed.

## Chapter 4

# HIFU Transmitter IC Design and Implementation

The IC to be used in the integrated HIFU system of Fig. 1.5 must have a maximum width equal to the catheter diameter of 2 mm. For packaging considerations of the system in catheter, the layout and placement of eight output stages should be done in a row such that output pads can be easily accessible for wire bonding to input pads of CMUT elements. The sizing of utilized metal layers in the layout of high power parts is based on the maximum allowable current density rules of AMS H35 (4M) process to increase the reliability of the chip. Also, in order to isolate the PLL and digital trigger pulse generator blocks from substrate noise generated by HV drivers, all high voltage transistors, blocks and the whole 8-channel HV driver are surrounded by appropriate guard rings.

### 4.1 Digital Pulse Generator

The 8-element equal area concentric CMUT array used in this study (shown in Fig. 1.4) focuses the acoustic beam to a specific distance from the center when is being driven by appropriate phased signals generated by pulse generator. Geometry of the CMUT device can also be depicted as Fig. 4.1<sup>1</sup>. Here,  $r_i = R \times \sqrt{i/8}$  where  $R$  is the outer radius of the transducer, and  $i = 0, 1, 2, \dots, 7$ . Relative phases for the element drive signals are found by calculating the respective path length differences  $d_i$  with respect to the central element. For the  $i^{th}$  transducer element,  $d_i$  is found as:

$$d_i = \sqrt{F^2 + r_{c,i}^2} - F \quad 4.1$$

Where  $r_{c,i} = (r_{i+1} + r_i)/2$  and  $F$  is the focal distance. Phase of  $i^{th}$  the drive signal is calculated as [44]:

---

<sup>1</sup> Reproduced with permission from co-authored publication: [44]

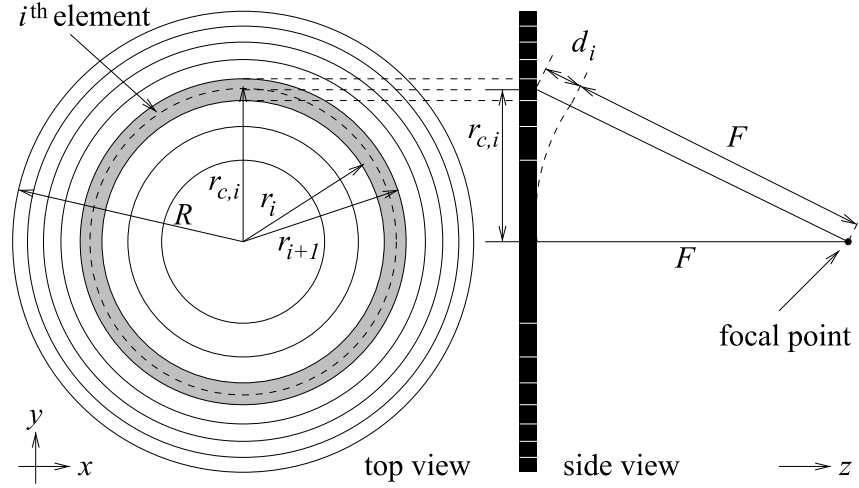


Figure 4.1: Geometry of the transducer array used in experiments.

$$\Phi_i \equiv 2\pi d_i/\lambda \text{ (mode } 2\pi) \quad 4.2$$

As the intended application for the IC is to drive continuous wave signals into a HIFU transducer, the digital pulse generator is expected to generate signals with phase difference, rather than time delay. Every channel of the device comprises two independent parallel loadable synchronous counters (Fig. 4.2). Start values for the counters are clocked serially in by the use of the SDA and SCL lines of a chain of shift registers with parallel data output. Counters are set to a starting count value by the assertion of the LOAD signal, which simultaneously starts all counters upon de-assertion. The two individual counters of a pulse channel are independently loaded, which is used to adjust the duty cycle. As each counter consists of four bits, DOUT <3> compensate for possible race conditions due to a delayed clock, DOUT <3> signals are delayed by the insertion of dummy XOR gates to the output path. Signals PH and PL are 180° out of phase trigger signals for the high voltage PMOS and NMOS drivers, respectively. Depending on the starting values loaded into the individual channel counters, their duty cycle may be varied in the interval 0%–50%. Consequently, they provide non-overlapping pulse signals. The duty cycle should be kept below 50% to compensate for the turn-off delay of the high-voltage MOS transistors. For an  $f_{CLK}$  value of 160 MHz, both counters produce a 10 MHz signal. Relative phases of the individual channels can be varied by 3.125 ns, which provide a phase resolution of 11.25°. Here for producing of 8-12 MHz trigger signals for HV

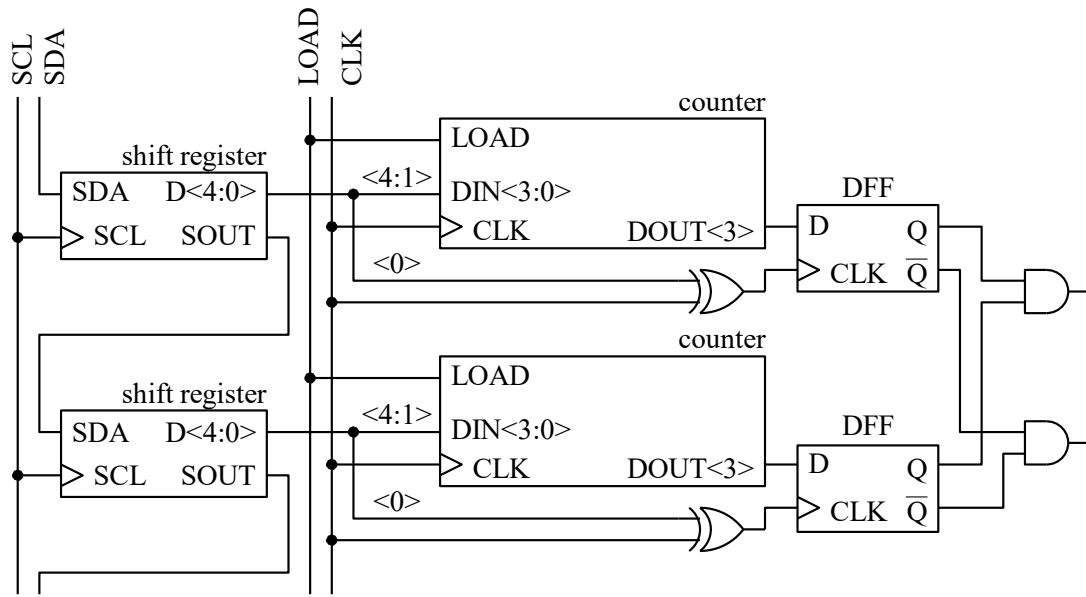


Figure 4.2: One channel of the digital beamformer. Two parallel loadable synchronous counters generate 50% duty cycle pulses, whose overlap can be adjusted by the initial count value to set the duty cycle of the output. The XOR gates acting as programmable inverters provide an additional half clock cycle phase resolution. PH and PL, which are always 180° out of phase, provide the drive signals for the PMOS and NMOS of the output driver, respectively. All data are shifted in serially.

drivers, the pulse generator should be fed by 128-192 MHz adjustable clock by a phase locked loop frequency synthesizer.

## 4.2 Phase Locked Loop

The integer-N PLL frequency synthesizer architecture is shown in Fig. 4.3. In order to define the bandwidth of the loop filter in a PLL, a trade-off should be made between spurs rejection and in-band phase noise. For higher values of loop bandwidth, the response of loop would be faster and in-band noise attenuation would be higher, however, spurs rejection performance would be weaker. Since HIFU exposure times are in seconds, and the frequency is not altered often, there is no fast settling time requirement on the PLL. Stability and accuracy of the output frequency of the PLL is a more important concern for the precision of HIFU ablation. Two important factors in defining the performance of a PLL system are damping coefficient ( $\zeta$ ) and natural frequency ( $\omega_n$ ) that can be calculated by following equations [63]:

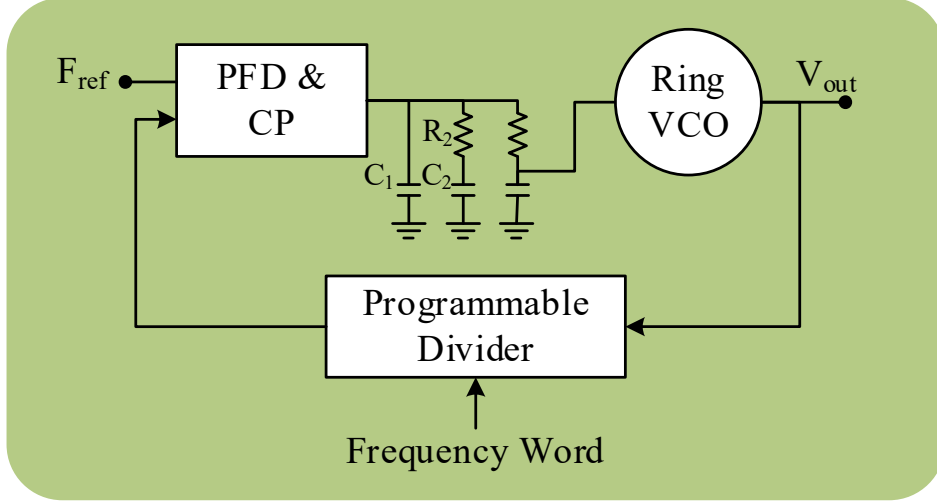


Figure 4.3: Functional block diagram of Integer-N PLL, which comprises a phase and frequency detector, and charge pump, the loop filter, a VCO, and a programmable divider.

$$\zeta = \frac{R_2}{2} \sqrt{\frac{I_P C_2 K_{VCO}}{2\pi M}} \quad 4.3$$

$$\omega_n = \sqrt{\frac{I_P K_{VCO}}{2\pi C_2 M}} \quad 4.4$$

Here,  $M$  is the divide ratio of frequency divider,  $I_P$  is the charge pump current and  $R_2$  and  $C_2$  are filter components. The output frequency would be  $f_{out} = N \times f_{ref}$ . In this design, in order to have highly stable output signal with low spur components,  $\zeta$  and  $\omega_n$  were chosen as 1 and  $2\pi \times (20.1 \text{ kHz})$ , respectively. Also, to have a reasonable size for on-chip passive elements of loop filter, charge pump current is set to  $1.1 \mu\text{A}$ .

#### 4.2.1 Capacitive-Tuned Ring VCO

Ring VCOs are popular for their high tuning range and small footprint. Despite their weak phase noise performance compared to LCVCOs, their capability to operate at sub-GHz frequencies make ring VCOs a more suitable candidate for biomedical [64], biological [65], [66] or any relatively low frequency applications. The oscillation frequency of ring oscillator is defined by the number of stages ( $N$ ) and propagation delay  $\tau_d$  per stage and is given by [67]:

$$f_0 = \frac{I_{cont}}{2NV_{osc}C_L} \quad 4.5$$

Where  $\tau_d = V_{osc}C_L/I_{cont}$ ,  $V_{osc}$  is the oscillation voltage amplitude,  $C_L$  is the total capacitance at the input/output of each stage and  $I_{cont}$  is the current passing through each CMOS cell.

Eq. 4.5 implies that the oscillation frequency of the ring VCO can be controlled by the number of stages, supply voltage, size of transistors (or any additive capacitance or resistance between stages) and by adjusting the current through each cell. The frequency range of the VCO is limited to 128-192 MHz, as wider tuning range will increase the sensitivity of the VCO to any voltage-induced phase noise.

Since the high power pulser blocks already consume considerable power, a low power design approach is not assumed for the design of the PLL and VCO blocks. Instead, lower chip area and better phase performance are preferred. A nine-stage inverter-based capacitive-tuned ring VCO is used in the circuit (Fig. 4.4). Among the nine inverter stages, six of them are loaded with delay controlling stages, each of which contain a fixed capacitor in series with an NMOS transistor acting as a voltage-controlled resistor. One stage, on the other hand, has a fixed capacitor as load to set the center frequency. Use of variable load capacitors instead of variable inverter currents provides better phase noise performance at the price of increased power consumption [68].

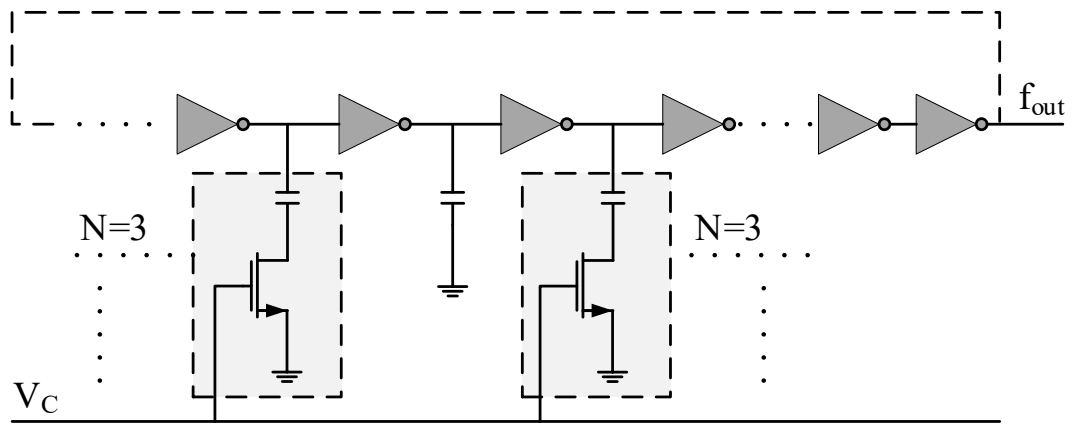


Figure 4.4: Simplified schematic of proposed ring VCO. While six out of nine inverters are loaded with variable capacitors, one has a fixed output capacitor to set the tuning range.

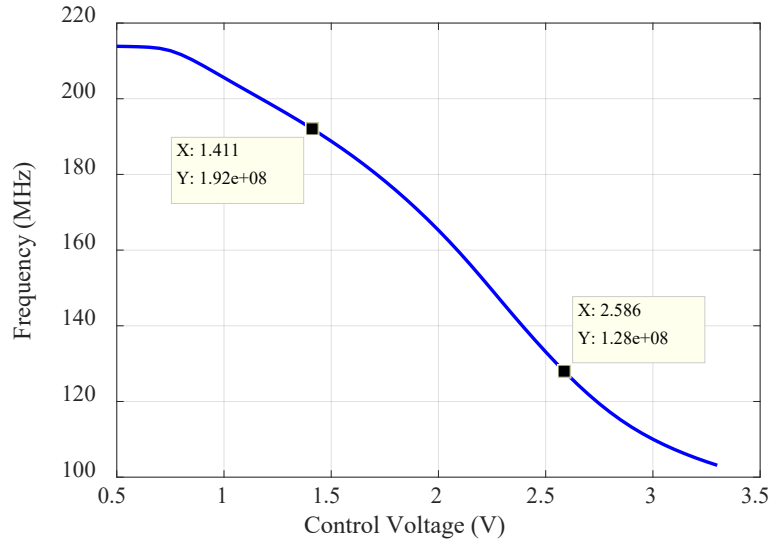


Figure 4.5: Measurement result for the open-loop VCO gain within the tuning range. To account for process corner variations, the tuning range is kept slightly larger than the desired range of 128–192 MHz.

In order to obtain a linear VCO gain, the length (L) of NMOS transistors is chosen to be large to decrease the sensitivity of channel resistance to the control voltage of VCO. The desired frequency range for the proposed VCO is obtained by setting the tuning NMOS dimensions as  $W=15\ \mu\text{m}$  and  $L=5\ \mu\text{m}$  and using a series capacitor of value 560 fF. The fixed capacitor has a value of 135 fF. The VCO gain is measured as 54.5 MHz/V (Fig. 4.5).

## 4.2.2 Phase/Frequency Detector and Charge Pump

A Nand-based phase and frequency detector (PFD) shown in Fig. 4.6 is considered for the PLL. The PFD which is actually implemented by two D Flip-Flops and a Nand gate in reset path compares the frequency divider's output with the reference clock. This topology is the most capable and well-known PFD proposed in [63] appropriate for the frequencies below 500 MHz. The capacitance in the reset path is used for eliminating the dead-zone of charge pump and VCO path. Dead zone happens when the phase difference ( $\Delta\Phi$ ) between the reference clock and that of divider is such low that is not detectable by charge pump leading to no current injection to the loop filter and the control voltage of VCO. It makes the PLL working as an open loop system and allows the VCO to

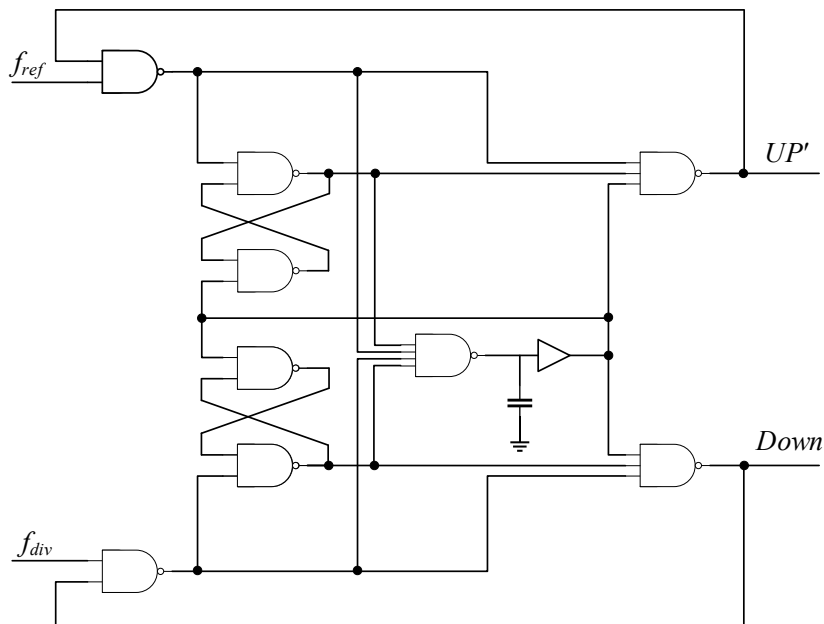


Figure 4.6: Gate-level schematic of Nand-based phase and frequency detector

accumulate substantial random phase errors called jitter.

In addition to dead zone, the other issue in PLL loop components is the mismatch between the currents of output stage transistors of the charge pump. When the PLL is locked, the net injected current from charge pump should be zero, but in the case of current mismatch, PLL will generate phase error to keep the net current zero and the loop remaining locked. A possible solution is to increase the length of the last stage transistors of the charge pump to decrease the channel length modulation effect, which improves the conformity of up and down signals [69]. This method, however, negatively affects the speed and linearity of the charge pump and increases the in-band phase noise. In [70]

feedback transistors are employed to overcome this problem ( $M_{FP}$  and  $M_{FN}$  of Fig. 4.7). A rise in the output voltage results in an increase in Down, and decrease in Up currents, due to the channel length modulation effect. In parallel, an increase in the output voltage increases  $V_F$  that puts  $M_{FN}$  into deep triode region. Consequently, the ON resistance of  $M_{FN}$  gets smaller which will result in a decrease in the mirrored current at the main branch. Similarly, the compensation is done by  $M_{FP}$  for a decrease in output voltage. The post-layout simulation result in Fig. 4.8 indicates that there is almost two-fold improvement in normalized current mismatch error when feedback transistors are employed.

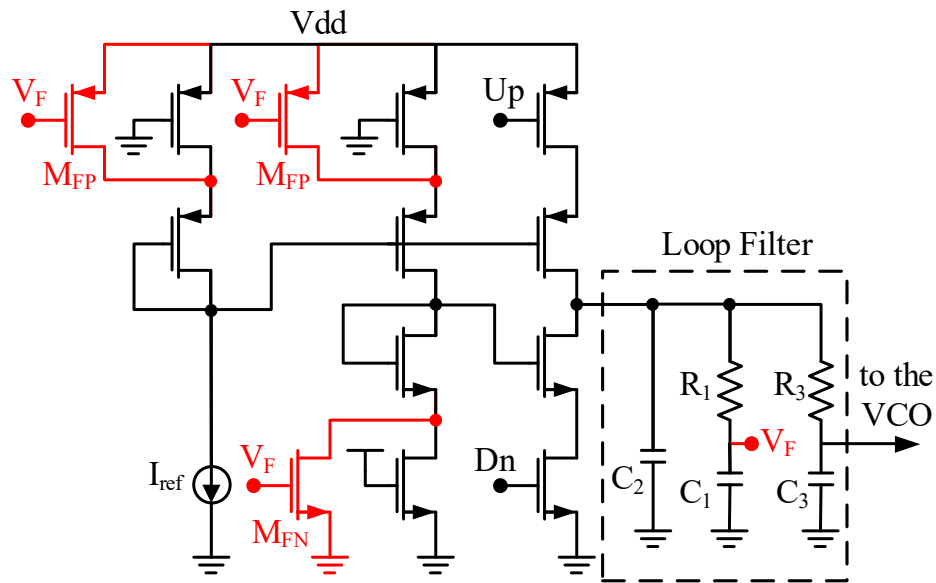


Figure 4.7: Circuit schematic of the charge pump, with  $M_{FP}$  and  $M_{FN}$  feedback transistors added to compensate the up and down current mismatch.

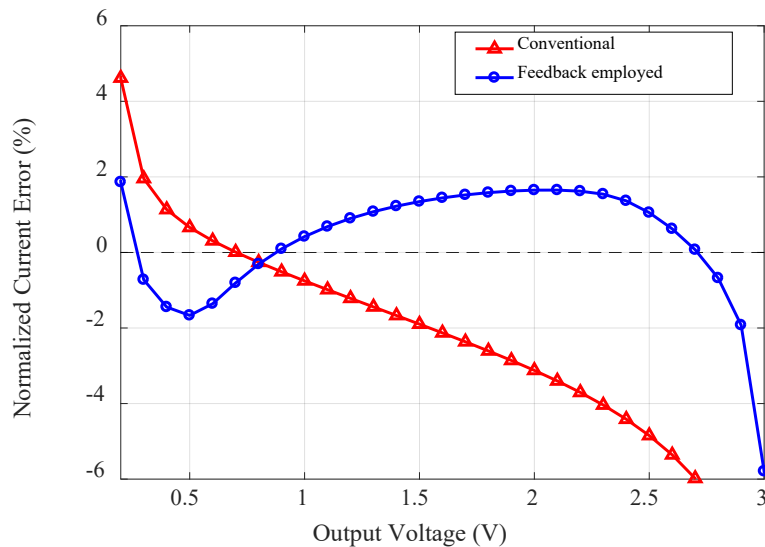


Figure 4.8: Normalized current error of charge pump circuit. Feedback reduces the

### 4.2.3 Frequency Divider

Fig. 4.9 shows a simplified diagram of the programmable frequency divider used in the feedback loop of the PLL. The modular structure consists of a chain of 2/3 divider cells connected like a ripple counter [71]. The main advantage of this structure is the utilization of the same sub-blocks, simplifying design and layout steps. The elimination of the global feedback loop by replacing it with local feedback lines ( $Mod_{in}$  and  $Mod_{out}$ ) between each 2/3 divider block will result in smaller power consumption compared to swallow type dividers [72]. Based on the situation of the inputs  $Mod_{in}$  and  $P_n$  the divider cell divides by 2 or 3. When  $P_n$  is low, the first stage divides by two. The  $Mod_{in}$  signal of the last stage is always high, ensuring that all stages divide by two when their input bits  $P_n$  are low. For dividing by 3, the signals  $Mod_{in}$  and  $P_n$  should be high. The divide ratio can be varied between  $2^N$  and  $(2^{N+1} - 1)$  when all  $P_i$ s are low and high, respectively, where  $N$  is the number of stages. A five-stage divider is used for this PLL, as the desired divide ratio is between 32 and 48.

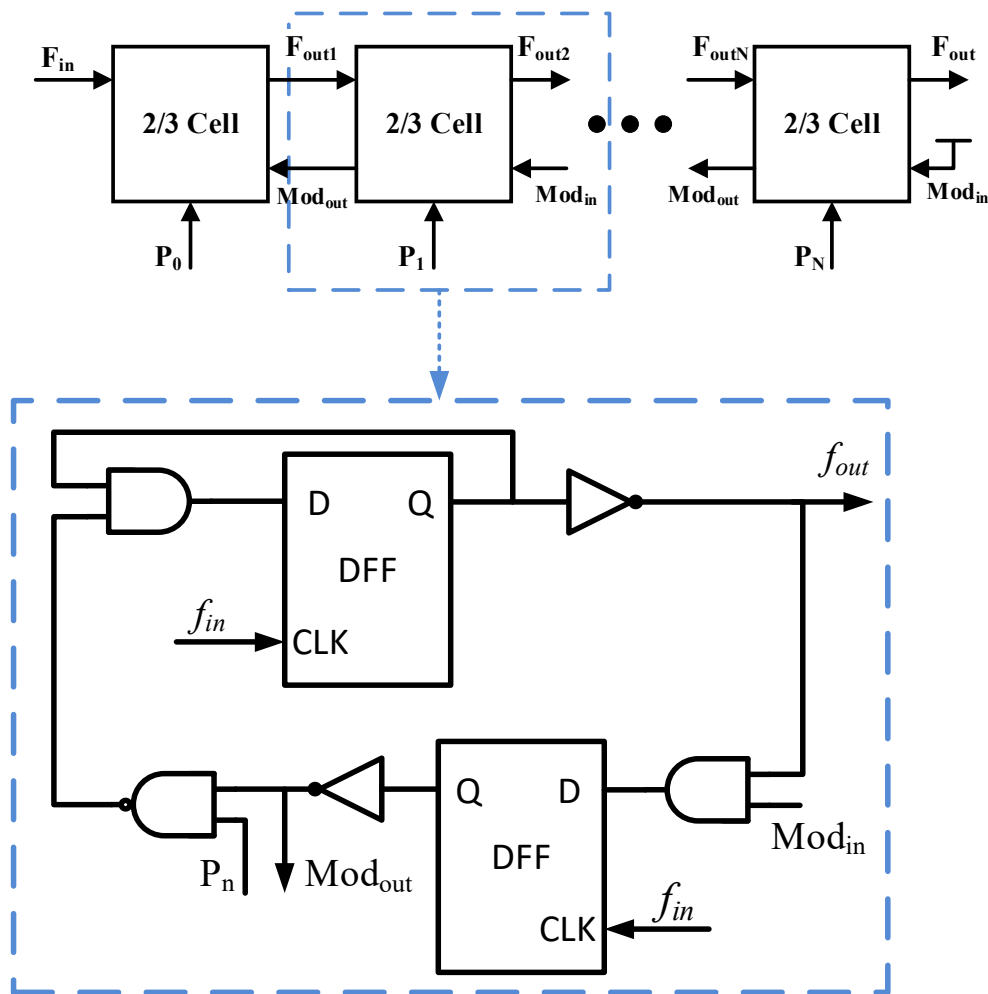


Figure 4.9: Schematic of frequency divider.

### 4.3 High Voltage Driver Array

The push-pull architecture is the most commonly used topology for HV and high-speed ultrasound transducer drive applications. Schematic of the designed HV driver is shown in Fig. 4.10 The circuit is essentially a high-voltage CMOS inverter. The challenge in the design is the level-shifting of the PMOS control signal as to limit the gate voltage of the driver to comply with the maximum gate-to-source voltage specification of the process.

As reported in the literature, either current mirror based level shifters [56], [73] or latch type cross-coupled structures [53], [74], [75] are used to translate the low voltage trigger pulses to appropriate pulses for driving the PMOS. All these designs are performed based on the system requirements for their specific applications and characteristics of related transducer. The current mirror based structures suffer from high dependency of their rise time to temperature and process variation and have low transition speed. This dependency limits the maximum load drive capability and maximum operation frequency and may put stress on the HV PMOS transistors. The cross coupled structure, on the other hand, can operate at higher frequencies, but it is not a good candidate for a CW application due to its high static power consumption.

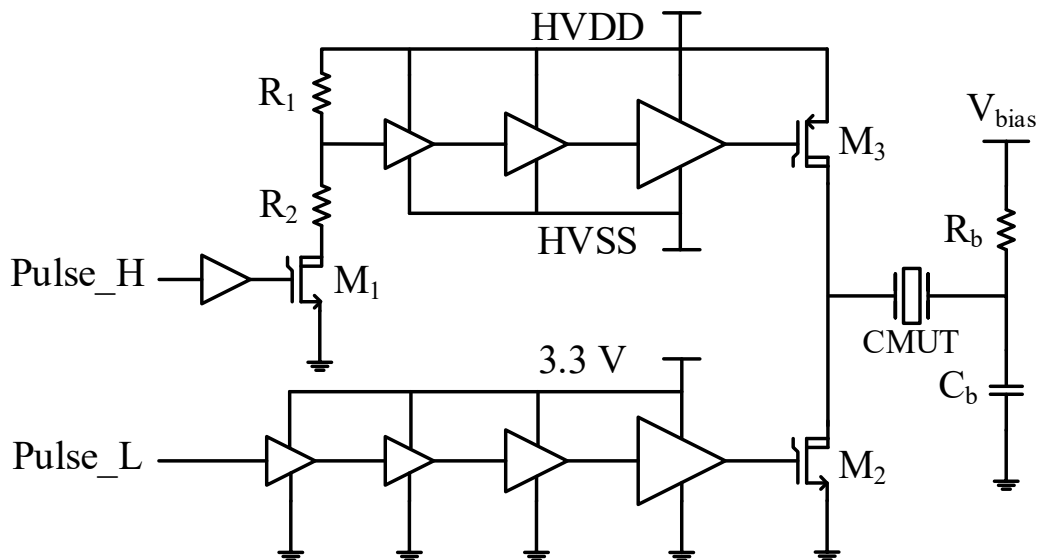


Figure 4.10: Circuit schematic of proposed High-Voltage pulser.  $Pulse\_L$  and  $Pulse\_H$  signals, which are generated by the digital beamformer, pass through super buffers to be able to drive the large sized output transistors.

In this circuit, a resistive divider-based voltage level-shifter followed by a super buffer is designed as the driver part of the HV PMOS transistor. For level shifting, two high resistivity polysilicon resistors,  $R_1$  and  $R_2$  along with a HV NMOS,  $M_1$ , are employed as shown in Fig. 4.10. By this method the level shifted trigger pulse for  $M_3$  depends on the ratio of the resistor values only and is independent from process or temperature variations.  $R_1$  and  $R_2$  are chosen to be large enough for keeping the dissipated power as low as possible. Their ratio is defined such that the HV driver can produce HV pulses from  $15 V_{pp}$  to  $50 V_{pp}$ . According to the post-layout simulations, one HV driver channel dissipates only 2 mW for level-shifting and buffering of the trigger pulses. The HV transistors,  $M_1$ ,  $M_2$  and  $M_3$  are thin oxide transistors with fast switching performance. Width of  $M_2$  and  $M_3$  are  $400 \mu\text{m}$  and  $700 \mu\text{m}$ , respectively. Conventionally, the PMOS transistor of a CMOS inverter has a size of 2 to 3 times of that of the NMOS, but in this design the size has been reduced to save area and to decrease the output node capacitance. According to simulations in Cadence, Virtuoso, for a PMOS of width  $1000 \mu\text{m}$  the additional capacitive load seen at the output node could cause an additional 2 mW higher power consumption for each HV driver channel at 12 MHz comparing with  $700 \mu\text{m}$  transistors whose size is already enough for the maximum allowable current density needed for driving of our CMUT array. As the drive path and DC supplies of high-voltage  $M_2$  and  $M_3$  transistors are different, the reduced rise time due to the smaller size of  $M_3$  can be compensated by increasing the overdrive voltage of the PMOS with an adjustment to HVSS. Fig. 4.11 shows the layout view of a single HV driver.

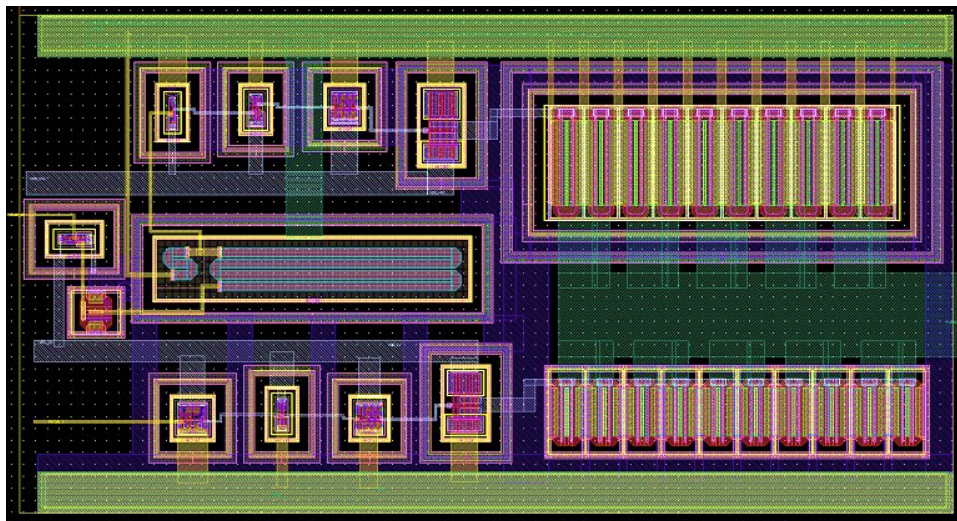


Figure 4.11: Layout view of single HV driver cell.

## 4.4 Analog Pulse generator

Considering that an N-stages ring VCO can generate  $(360/N)$  degree phase difference between adjacent delay elements, in the second chip a PLL with an eight-stage differential ring VCO was designed to produce 16 different phased signals (with  $22.5^\circ$  phase resolution) to trigger the HV drivers.

The PFD, charge-pump and frequency divider blocks used in the 8-12 MHz integer-N PLL of analog pulse generator are similar to those of used in the 128-192 MHz of the first chip. In the next part VCO and loop filter design will be explained.

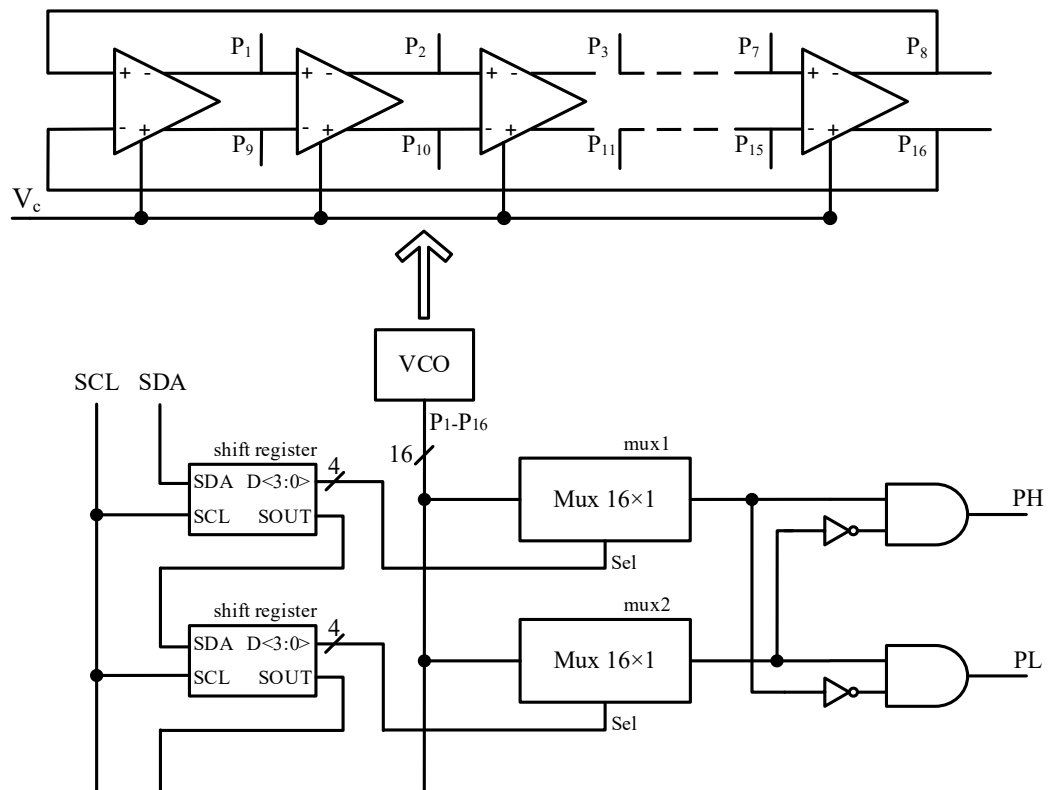


Figure 4.12: The differential ring VCO used in transmit beamforming circuit for one channel. Any of the 16 generated signals by VCO can be fed to the HV driver. Duty-cycle of non-overlap PH and PL can be adjusted by appropriate combination of the VCO outputs.

#### 4.4.1 Differential Ring VCO

An 8-stage symmetric-load delay cell based differential ring VCO operating between 16-24 MHz was designed for the analog phase generator. The symmetric MOS load would approximate voltage-controlled resistor while providing a linear VCO gain [76]. Since threshold level of the differential delay cell cannot be exactly adjusted as  $V_{dd}/2$ , and as a result the duty cycle of 50% could not be obtained for the clock phases, the operation frequency of core VCO is twice the interested frequency. 16 divide-by-two counters guarantees the 50% duty cycle at 8-12 MHz. Additional frequency range was considered to compensate the fabrication and corner non-idealities. The schematic of a symmetric-load delay cell is shown in Fig. 4.13. Considering that any mismatch in the layout of cells could lead to error in the produced phases, a symmetric and careful layout with large transistors was performed in the design of delay cell based VCO. Symmetric loads consist of a diode-connected PMOS device parallel with an equally sized PMOS device. The PMOS bias voltage is  $V_c$ , the control voltage from loop filter.  $V_c$  defines the lower voltage swing limit of the buffer outputs. The buffer delay changes with  $V_c$  since the effective resistance of the load elements also changes with it [76]. Fig. 4.14 shows the post-layout simulation result of VCO gain (after dividing the frequency by two). According to equations 4.3, 4.4 and VCO gain,  $K_{VCO}$ , the filter components can be defined.

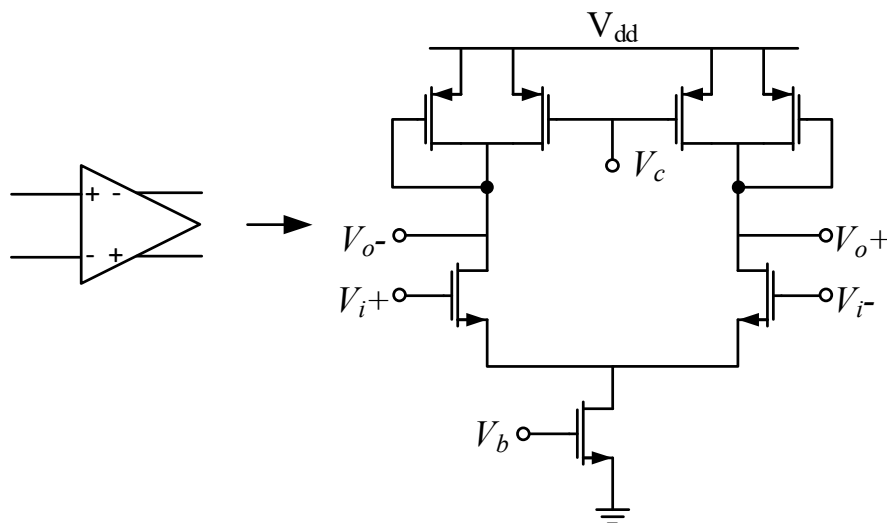


Figure 4.13: Schematic of single delay cell used in VCO. A pair of 500 fF capacitors at outputs of each cell are used to decrease the phase errors due to non-equal routes of output clocks.

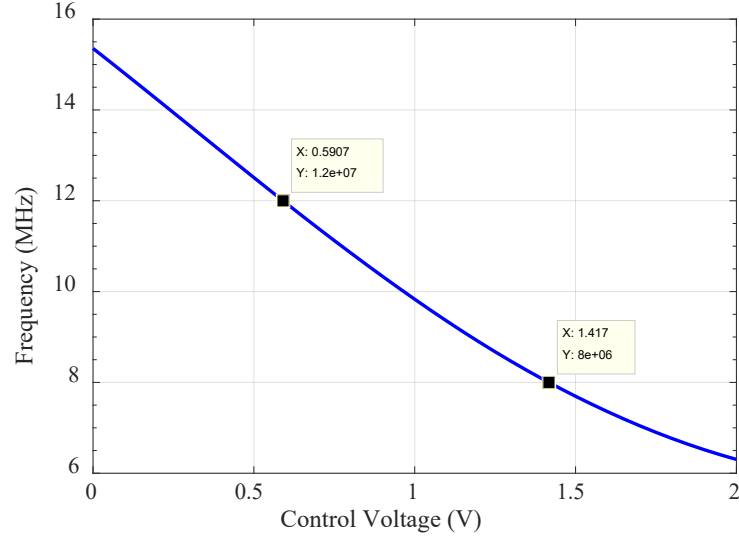


Figure 4.14: Post-layout simulation result of delay-cell based fully differential ring VCO.

#### 4.4.2 Loop Filter

Relatively low operation frequency of PLL needs large off-chip components for loop filter. In this PLL, again higher loop stability and higher reference noise suppression have more priority than fast lock performance. For a low bandwidth loop with high stability, the charge pump current was set to  $1.1 \mu\text{A}$ ,  $\zeta$  and  $\omega_n$  were chosen as 1 and  $2\pi \times (500 \text{ Hz})$ , respectively. For obtaining these parameters,  $C_2$  and  $R_2$  (Fig. 4.3) have to be around  $2.4 \text{ nF}$  and  $240 \text{ K}\Omega$ , however implementing a very bulky  $2.4 \text{ nF}$  capacitor as an on-chip component is almost impossible. Because of the catheter-based application of the final device, off-chip components are not good option for loop filter. the possible way is to use a CMOS capacitor multiplier which can play the same impedance effect as our interested capacitor. Here as shown in the Fig. 4.15 a current mirror based ( $\times 20$ ) capacitance multiplier was designed for the frequency range of loop filter. The current passing the capacitor is sensed by  $MN_0$  and is mirrored by 1:19 (M) gain by  $MN_1$ . This amplified current is then drawn by the (+) node. By this technique, any voltage change on the capacitor will create a current in it whose M times passes also from  $MN_1$  which results in an impedance of  $(M+1)^{-1}$  times in the input. This means the input capacitor would be equal to  $C \times (M+1)$  in a specific range of frequency. It should be noted that a capacitor multiplier does not show ideal operation in all frequencies; in lower frequencies

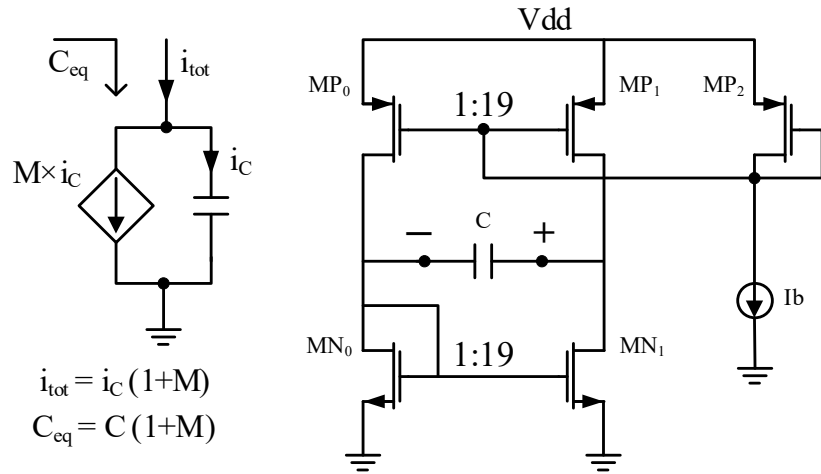


Figure 4.15: Conceptual (left) and circuit schematic (right) of capacitor multiplier.

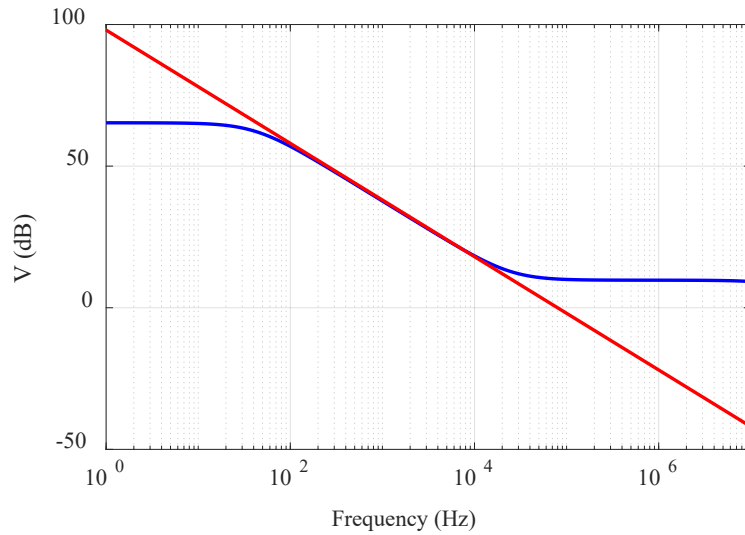


Figure 4.16: Frequency response of low-pass filter: with ideal 2.4 nF capacitor (red), with  $20 \times 120$  pF capacitor multiplier (blue). The circuit designed for operation between 0.1-10 KHz, appropriate for the loop filter function.

the impedance of the output impedance of the circuit is limited by the output resistor of  $MN_1$  [77].

As a result, in the frequencies lower than  $\omega = 1/(r_{oMN_1}(M + 1)c)$  the circuit will show resistive effect. Also, at high frequencies, the capacitance is limited to  $C$ . Fig. 4.16 shows a comparative ac sweep analysis of a low-pass filter with ideal capacitor and its equivalent capacitive multiplied component which indicates the design was performed for operation in 0.1-10 KHz frequency range.

## Chapter 5

### Chip Measurement and HIFU System

#### Characterization

As mentioned earlier, in this study two chips with same HV driver array and different phase shifting topologies for HIFU phased-arrays were implemented. Both presented HIFU driver ICs are fabricated using 0.35  $\mu\text{m}$  AMS HV CMOS technology. Fig. 5.1 shows the micrograph of the chips.

Total size of each chip (including the IO pads) is  $1.85 \times 1.8 \text{ mm}^2$ . Functional blocks of two ICs (and their respective die areas) are a 128–192 MHz integer-N PLL ( $805 \times 305 \mu\text{m}^2$ ), a digital pulse generator ( $147 \times 1270 \mu\text{m}^2$ ), an eight-channel HV CMUT driver ( $8 \times (208 \times 392 \mu\text{m}^2)$ ) and an analog pulse generator ( $630 \times 820 \mu\text{m}^2$ ). Width of the chips are small enough to be placed on the catheter.

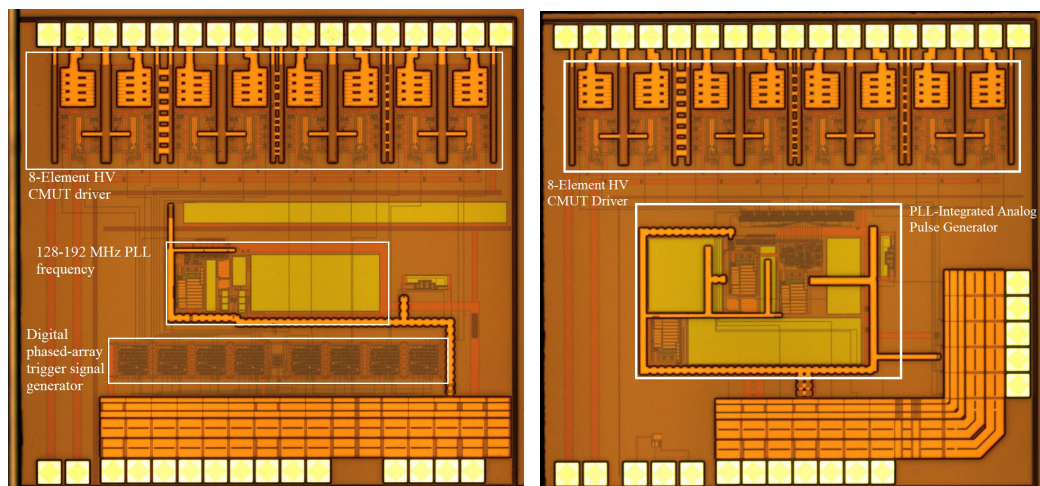


Figure 5.1: Micrograph of the two manufactured driver ICs. HIFU transmitter IC with 128-192 MHz PLL as reference clock generator, digital trigger pulse generator, 8-element HV driver array (Left). 8-12 MHz Analog pulse generator and 8-element HV driver array (Right).

## 5.1 Phase Locked Loop

The VCO frequency in free running mode spans the interval 105–210 MHz when the control voltage is varied between 0.7 V and 3.0 V. Fig. 5.2 shows the step response of the PLL, which is observed by measuring the control voltage of the VCO when the PLL is locked from a higher frequency to a lower one. This measurement has a settling time of about 370  $\mu\text{s}$  and an overshoot of 7%. The maximum measured power consumption of the PLL is 4.4 mW after the deduction of active IO pad consumption. The plot in Fig. 5.3 is the spectrum of VCO output with  $-40$  dBc reference-spurs rejection ratio when PLL is locked at 128 MHz.

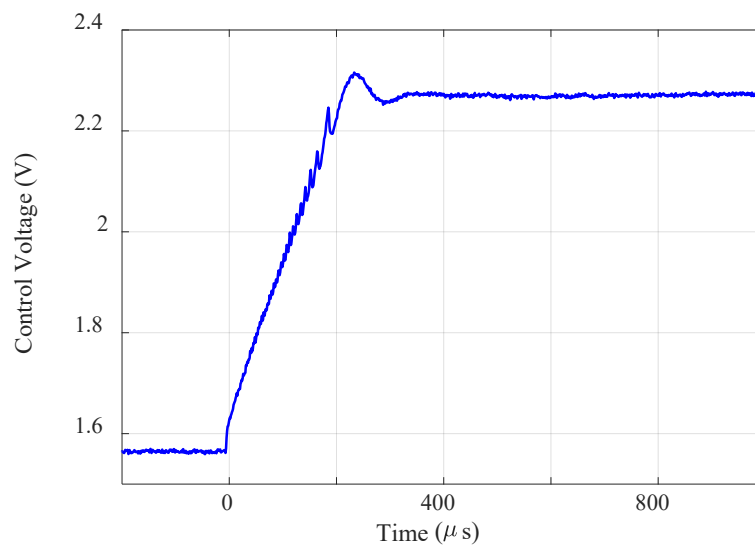


Figure 5.2: Step response of PLL seen from control voltage node of VCO.

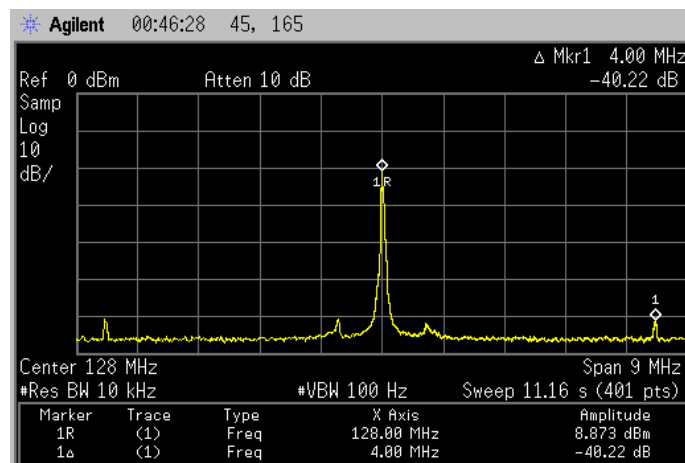


Figure 5.3: Output spectrum of PLL when locked at 128 MHz.

Fig. 5.4 shows the phase noise of PLL operating at 128 MHz at 10 kHz, 100 kHz and 1 MHz offset from center frequency. According to the phase noise equation of ring



Figure 5.4: Phase noise of PLL locked at 128 MHz.

VCOs presented in [68] and [78], capacitively tuned VCO approach improves the phase noise performance of the PLL with the cost of higher power consumption.

## 5.2 Digital Pulse Generator

Trigger signals generated by the pulse generator are expected to be internal signals for the final product version of the IC, but they are brought out for test purposes by the addition of I/O pads. Fig. 5.5 shows the PH and PL signals of the 1st and 5th channels of the beamformer. The set delay is 4 half cycles of the 160 MHz master clock (12.5 ns).

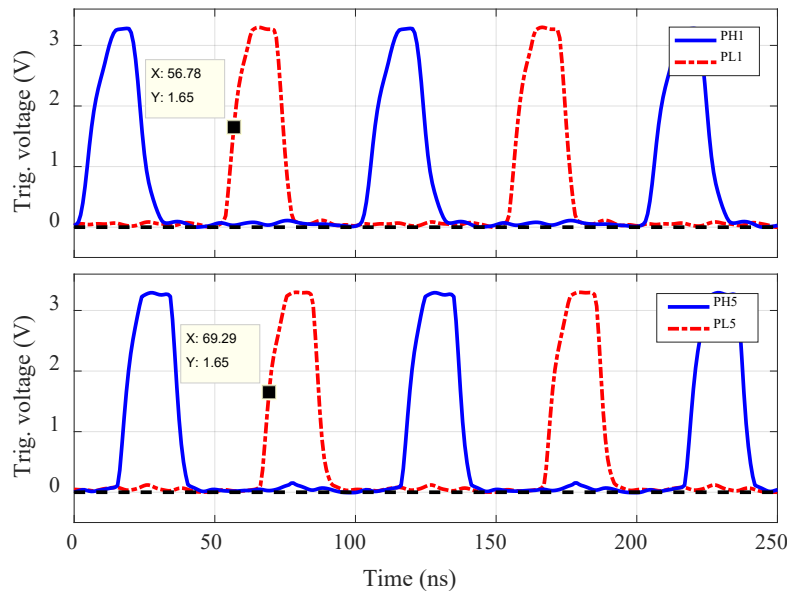


Figure 5.5: Measured PH and PL output for the 1st and 5th channels of the digital beamformer at 10 MHz. PH and PL are internal signals of the IC, but they are brought out on the prototype IC for test purposes. The duty cycle is 30%.

### 5.3 High Voltage Driver

The total power consumption of the driver section is measured as 545 mW and 664 mW at 10 MHz and 12 MHz, respectively, when driving 20 V<sub>pp</sub> pulses. A simulation run in Cadence Spectre at 10 MHz using the electrical model of the CMUT indicates that 130 mW of acoustic power is delivered to the load at a bias voltage of 130 Volts. This value is consistent with the FEM simulation result of 395 kPa RMS pressure at the transducer surface, for which the power radiated from a circular cross section of 1 mm radius into a radiation medium with 1.5 MRayl characteristic impedance is found as 160 mW.

The HV driver array is also tested with 10 MHz phased trigger signals with 11.25° phase difference for adjacent channels. The expected phase difference of  $11.25^\circ \times 4 = 45^\circ$  between output pulses of channels 1 and 5 is shown in Fig. 5.6 The rise and fall times of the HV pulses are 10.9 ns and 9.4 ns, respectively, when driving the 15 pF capacitance of the oscilloscope probe at 10 MHz. The same measurement is also performed at the supply voltage limit of 50 V for the particular CMOS technology. The rise and fall time for 50 V<sub>pp</sub> pulses at 10 MHz are measured as 12.5 ns and 15.5 ns, respectively. Table 5-1 presents a comparison between designed HV driver and similar works in literature.

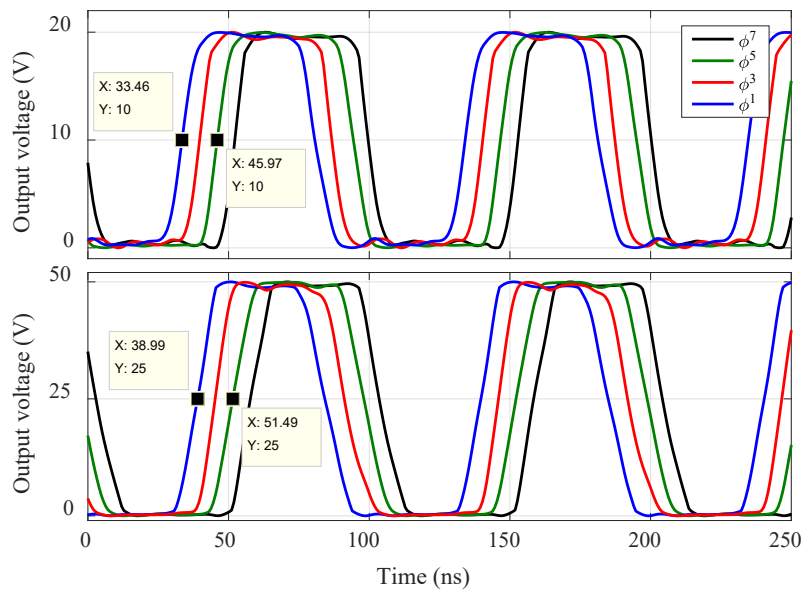


Figure 5.6: 20 V<sub>pp</sub> and 50 V<sub>pp</sub> pulses at the outputs of the odd numbered HV drivers measured by 15 pF oscilloscope probe  $4 \times 11.25^\circ$  phase difference at 10 MHz.

Table 5-1: Comparisons of the experimental results of the HV driver (single channel).

Parameter	[75] (2007)	[74] (2013)	[73] (2016)	This Work
Technology ( $\mu\text{m}$ )	0.8	0.18	0.35	0.35
Input Voltage (V)	5	1.8	3.3	3.3
Output Voltage (V)	59	9.8-12.8	30	20/50
Output Load (pF)	20	15	18	15
Frequency (MHz)	5	1.25	1.38	8-12
Rise/Fall time (ns)	69/58	40/50	68/65	10.9/9.4 (20 V) 12.5/15.5 (50 V)
Power (mW)	200 <sup>a</sup>	19.9 <sup>a</sup> 0.43 <sup>b</sup>	98	63 (20 V) <sup>c</sup> 377 (50 V) <sup>c</sup>
Chip area ( $\text{mm}^2$ )	0.85	0.022	0.08	0.08

<sup>a</sup> Simulated dynamic power.  
<sup>b</sup> Simulated static power.  
<sup>c</sup> Measurement at 10 MHz.

## 5.4 8-12 MHz PLL and Analog Pulse generator

Frequency step response of the PLL is shown in Fig. 5.7 which is related to the frequency change from 12 MHz to 8 MHz. The measured overshoot value is 11% and settling time is around 1 ms. Fig. 5.8 also shows a rejection ratio around 59 dB against 250 KHz clock signal generated at the output of PFD.

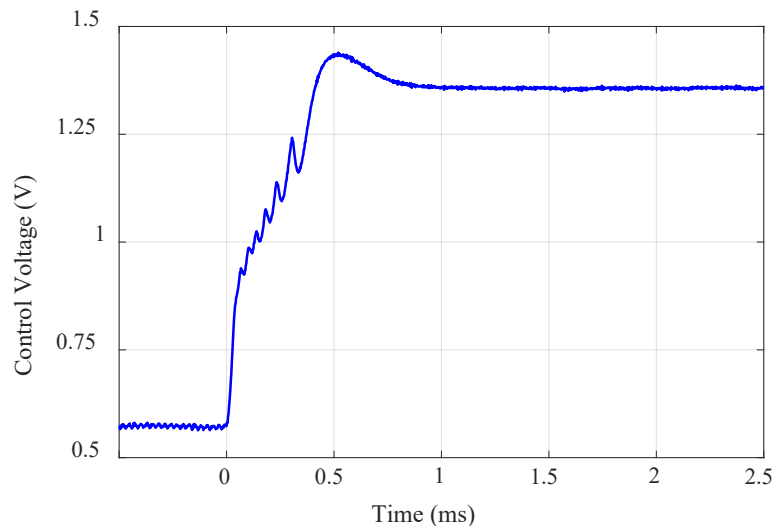


Figure 5.7: Frequency step response of PLL changing from the highest (12 MHz) operation frequency to the lowest (8 MHz). A phase margin around 64 degree had been considered in the design procedure.

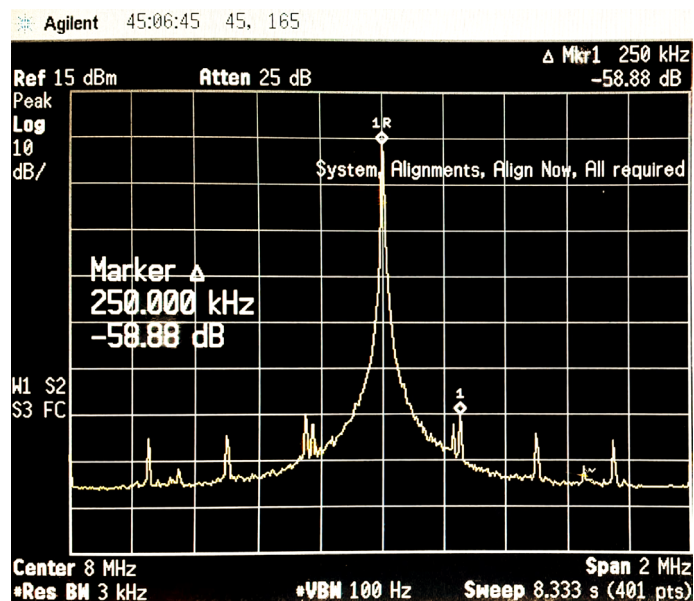


Figure 5.8: Output spectrum of PLL when locked at 8 MHz.

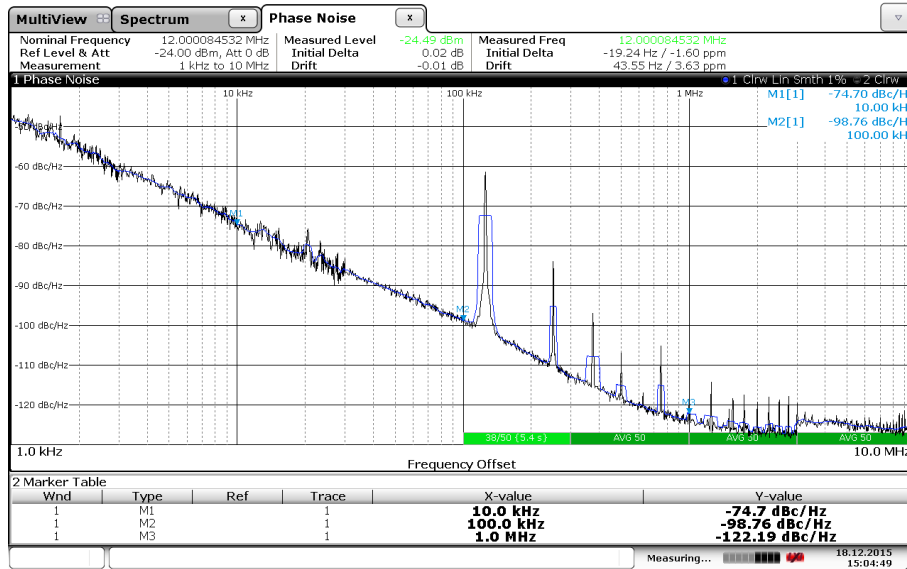


Figure 5.10: Phase noise of PLL locked at 12 MHz.

The phase noise of the PLL when locked at 12 MHz is also shown in Fig. 5.9. Also Fig. 5.10 shows the generated phased clocks for 4 channels of analog pulse generator. The operation frequency is 10 MHz and the  $22.5^\circ$  phase difference is equal to 6.25 ns in time.

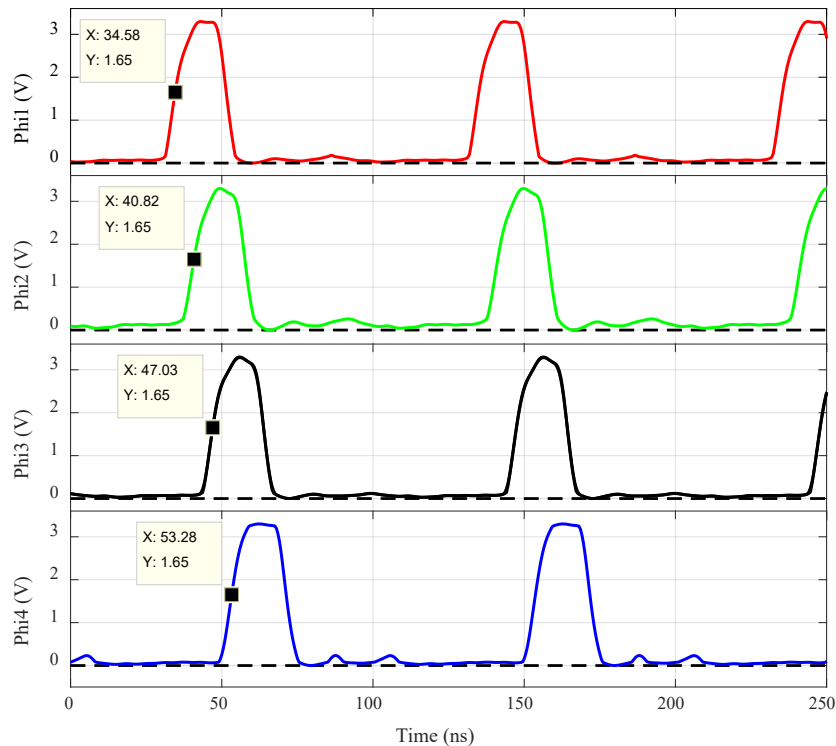


Figure 5.9: Measured phased clock for 4 adjacent channels. The duty cycle is 25%.

The total power consumption of the analog pulse generator and integrated 8-12 MHz PLL is around 2.2 mW excluding the active pads. Since the HV driver array is exactly the same as one used in the first chip, this block is not reported again.

## 5.5 Real-Time HIFU Beam Thermography

For characterizing the heating performance of the developed HIFU system and validate the safe and effective treatment, real-time information about focus depth and amount of delivered energy to an acoustically tissue-like medium would be very helpful. A conventional method is to test on HIFU phantom gel along with Magnetic Resonance Imaging (MRI) [79] which is costly; another method is to estimate the beam pattern and intensity using hydrophone and by mapping the pressure data to temperature which is complicated and [55] not accurate enough since the tip of a hydrophone will destroy the beam pattern and degrade the heating performance. There is also another thermal evaluation method introduced in [80] using Infrared (IR) thermography which provides the temperature seen from the top of the transducer, however, distance of the generated HIFU heat pattern from the transducer cannot be verified, and heat generated at the transducer surface cannot be discerned. In this study, we present a new method for IR thermography, in which the IR images were captured from a direction perpendicular to the HIFU field. This visualization technique provides real-time monitoring of HIFU and gives useful information about the temperature rise over time, beam pattern and focal distance. For this purpose, the transducer was placed in a tank of sunflower oil surrounded by appropriate and high transmittivity IR window.

As shown in Fig. 5.11, there are four radiation sources involved in the recorded temperature by an IR camera in non-contact infrared radiation (IR) thermography:

1. Energy reflected from the target and transmitted by the IR Window
2. Energy reflected from the IR Window
3. Energy emitted by the target and transmitted by the IR Window
4. Energy emitted by the IR Window

The first radiation is not possible since in our case, the HIFU beam is not a physical object and cannot reflect energy. The second and fourth sources were carefully cancelled by putting the test setup far from any energy source and in the same temperature as that of room.

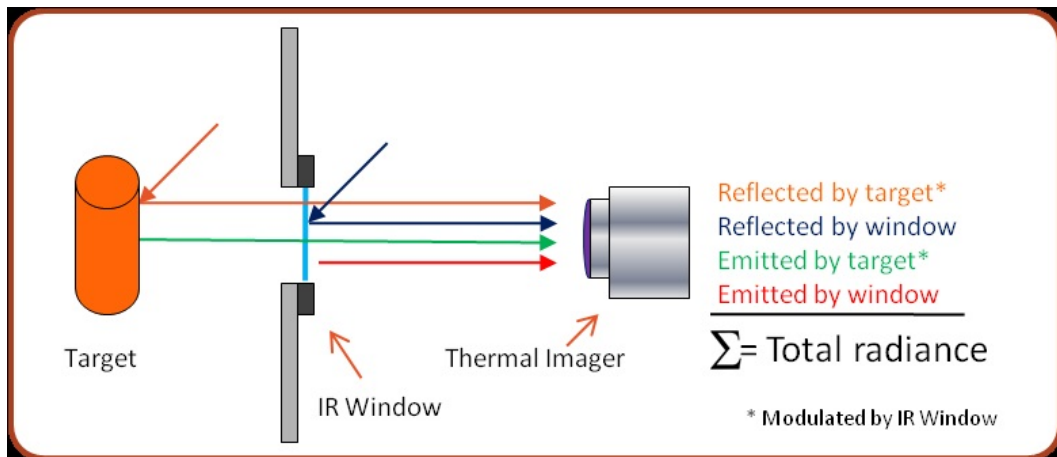


Figure 5.12: Radiance sources in non-contact IR thermography from a target. Reproduced from [81].

Therefore, the remaining source would be only the number three which is the emitted energy from the HIFU beam and transmitted by the IR window. In order to monitor the temperature rise in oil by an infrared camera, we used a 0.13 mm polyethylene film as an IR window for the walls of oil tank where the transducer is placed and being driven by the implemented HIFU transmitter IC. This material has around 80% transmissivity at our interested temperature wavelength ( $\sim 10 \mu\text{m}$ ) and makes real time temperature monitoring possible [82]. Fig. 5.12 shows the IR transmittance of the polyethylene film at different wavelengths and different thicknesses.

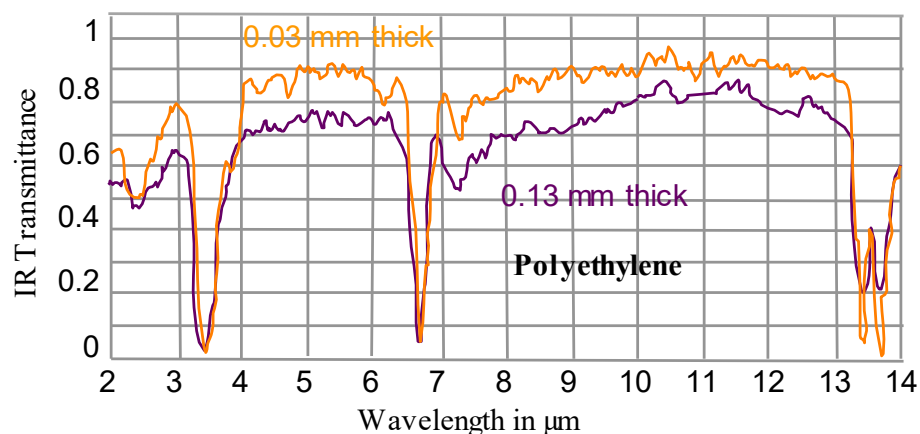


Figure 5.11: IR transmittance of polyethylene film at different wavelengths and different thicknesses. Reproduced and amended from [82].

The oil tank and test setup are shown in Fig. 5.13 The CMUT device is placed very close to the polyethylene wall such that the IR attenuation of oil becomes minimal. Fig. 5.14 shows the thermal images taken when the CMUT is focused to 6.7 mm distance and being driven by 20 V<sub>pp</sub> pulses at 10 MHz with 130 V DC bias.

The measurement reveals that the temperature at the focal point rises from 27.4 °C to 41.5 °C in just 11 seconds, which is a temperature difference in excess of 14 °C. By



Figure 5.13: The polyethylene oil tank placed on the PCB that holds the wirebonded CMUT array (left), IR camera monitoring the oil temperature while the transducer is driven by the IC (right).

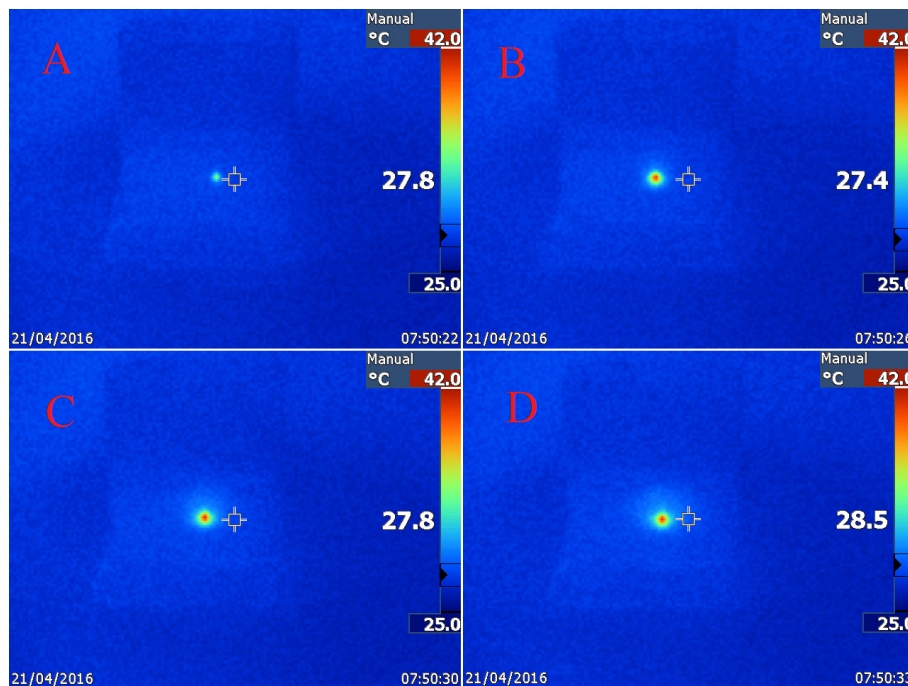


Figure 5.14: Progressive images of HIFU temperature spot taken in a 11 s. interval: A = 0, B = 4, C = 8, D = 11 s.

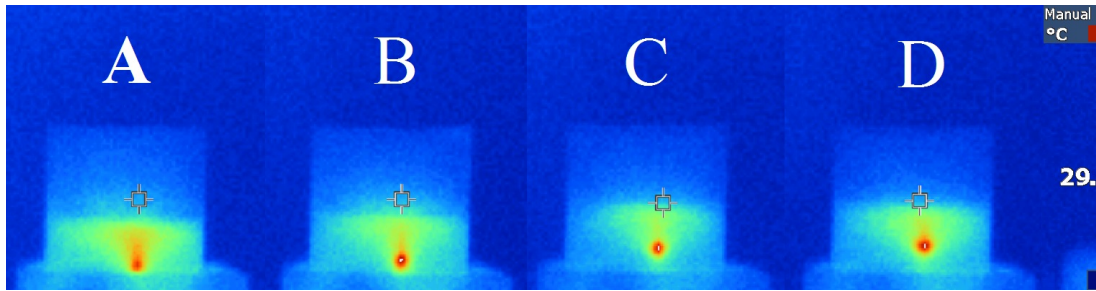


Figure 5.15: Observed HIFU thermal spot when focal point is set at (a) 2 mm, (b) 3 mm, (c) 4 mm, and (d) 5 mm.

compensating for the 20% attenuation of polyethylene layer (due to its 80% IR transmittance of the in 9–11  $\mu\text{m}$  wavelength [82]) the corrected temperature rise is found as 16.8  $^{\circ}\text{C}$  [83]. This measurement has only 2.2  $^{\circ}\text{C}$  difference with the preformed simulations by ANSYS discussed in Section III. It should be noted that this measurement is performed at room temperature, therefore, temperature rise started from 27.4  $^{\circ}\text{C}$ ; starting at a lower temperature (compared to the average human body temperature of 37.0  $^{\circ}\text{C}$ ) underestimates the heat generation. As attenuation of sound is higher at higher temperatures, higher amount of heat would be expected in living tissue [79].

When the system is evaluated using the  $\text{CEM}_{43}$  equation, we reach 594 equivalent minutes for only 20 seconds of HIFU operation of system. Considering that the system needs 11 seconds to 16.8  $^{\circ}\text{C}$  increase the tissue temperature, a total of 31 seconds operation of IC would be enough for producing a 594 equivalent minute thermal dose. According to [17], skin tissue is the least sensitive to thermal damage and its threshold for human is around 600  $\text{CEM}_{43}$ , however this threshold is 128  $\text{CEM}_{43}$  for myocardial necrosis [84]. Fig. 5.15 shows the observed thermal spot when the phase delays are adjusted to set the focal point to 2, 3, 4, and 5 mm.

## 5.6 *Ex-Vivo* Experiments on Ovine Liver

An ex-vivo experiment was also performed to evaluate the heating performance of proposed system. For this experiment, an ovine (sheep) liver slice of approximately 3 mm thickness was placed to the focal point of the CMUT array immersed in sunflower oil. The container was placed on a hot plate, and oil temperature was stabilized at 37  $^{\circ}\text{C}$ . The transducer was driven by the designed chip with 20  $V_{pp}$  pulses at 10 MHz. A thermal dose of 240  $\text{CEM}_{43}$  is required to cause cell death in liver [17]. This dose is reached in 8.1 seconds for a focal temperature value of 53.8  $^{\circ}\text{C}$ , which was measured by IR

thermography. The heating process requires another 11 seconds to rise tissue temperature from 37 °C to 53.8 °C. Consequently, about 19-20 seconds of system operation is expected to be sufficient. However, in our experiment we could not detect any lesion after 20 seconds of heating. By increasing the sonication duration (and replacing the slice with a new one for each experiment) the minimum exposure duration for appearing a lesion found to be slightly above 1 minute. This shows more exposure time is needed to generate a visible lesion on the tissue rather than that of calculated by the CEM<sub>43</sub> equation for the liver tissue thermal dose threshold, which is anticipated based on the results in [85]. A CEM<sub>43</sub> value of 240 is attained in 1 minute for a spot temperature of 51.3 °C. This experiment also verifies that the proposed system is able to ablate the target tissue within the 100 seconds time budget for safe catheter surface temperature (Fig. 3.5). The created lesion is shown in Fig. 5.16.

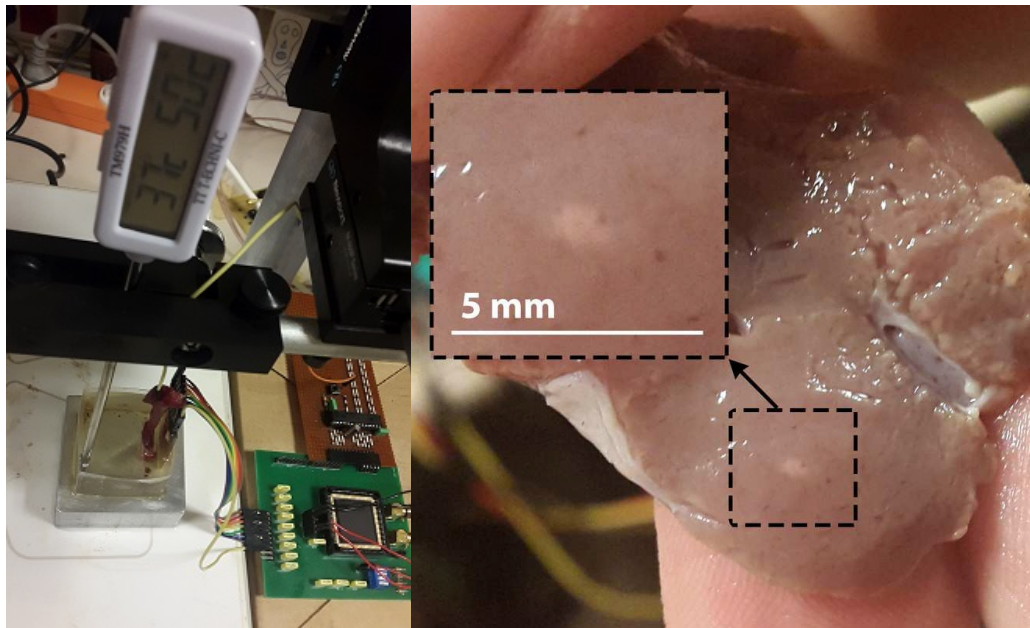


Figure 5.16: Setup for Ex-vivo experiment (left). Thermal lesion on ovine liver after one minute sonication (right).

## 5.7 Self-heating Assessment of Catheter Surface

As mentioned in section 3.2, the surface temperature of catheter can be elevated to temperatures higher than maximum allowable 42 °C due to considerable power dissipation during the HIFU operation. Since the blood vessel medium was not practically possible to provide for our lab experiments, a new ANSYS simulation was performed on the model of section 3.2 with oil, two-part epoxy and copper instead of blood, Polyurethane and silver respectively. It is expected that the new ANSYS simulation result to be similar to that of the experiment; therefore, the model in blood can also be true. Thermal parameters of the materials used in this simulation are listed in Table 5-2.

Also in the experiment, a 0.8 mm thick test PCB with 2.5 mm width is designed for placement of CMUT device and the transmitter IC. The copper rod heatsink under the chip is a 1.8 mm × 7mm and 35 μm thick trace on the back side of the pcb. The surface of PCB pads is coated with 200 nm of gold layer to ease the wire bonding. To stick the CMUT device and IC to the PCB, very thin layer of silver epoxy was used. Eight channel HV driver array of the chip is connected to the CMUT array and the power and signal pads are connected to the PCB by Kulicke and Soffa 4700AD wedge wire bonder at

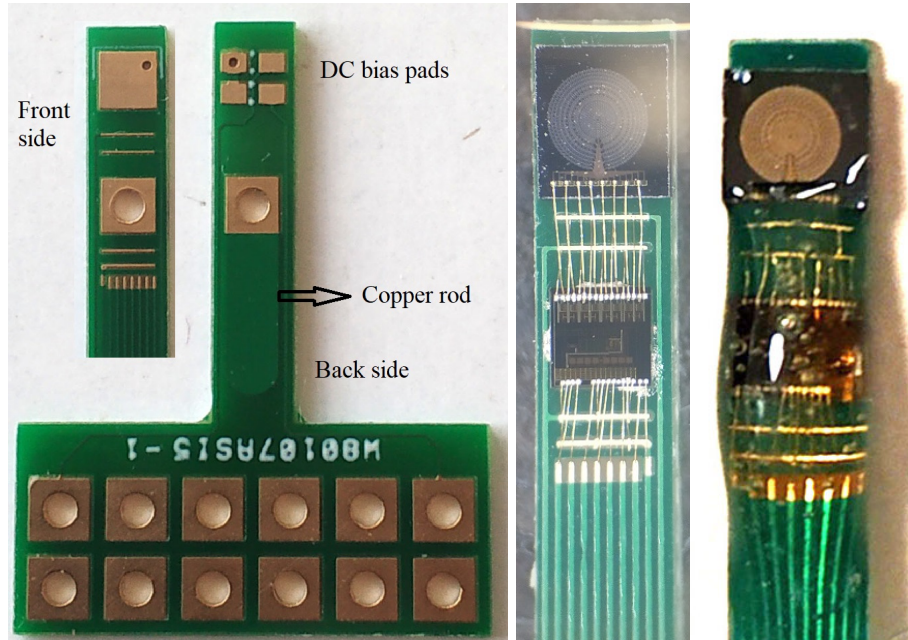


Figure 5.17: Designed PCB with 2.5 mm of width for self-heating assessment of HIFU transmitter IC with 350 mW power dissipation. Back and front sides (left). Wire-bonded chip to CMUT array and PCB signal and power pads (center). Two-part epoxy buried device (right).

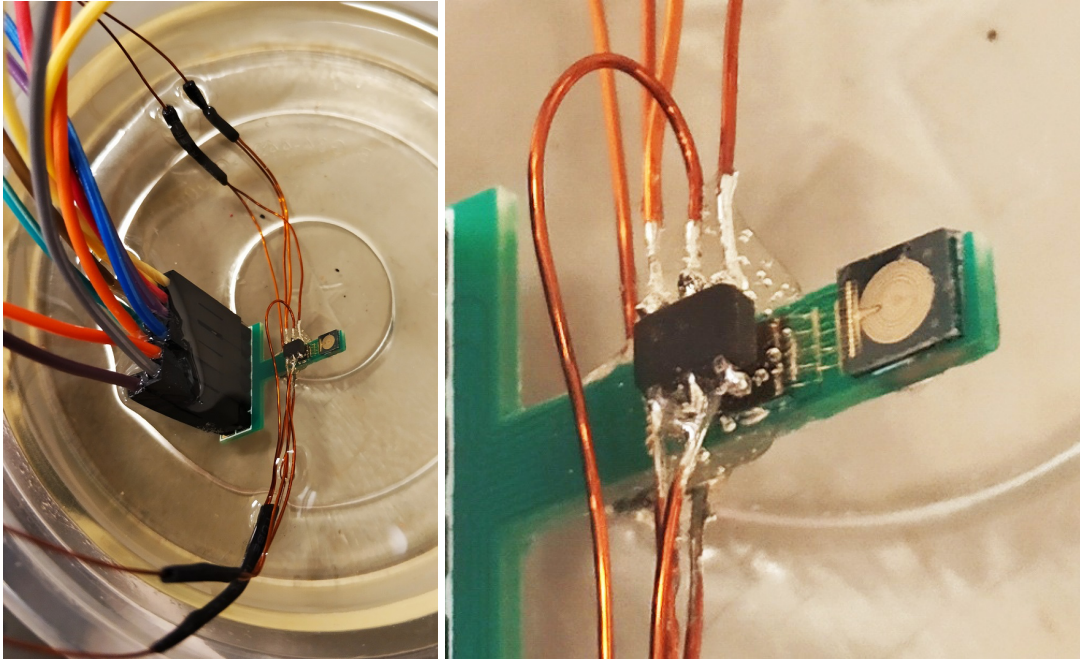


Figure 5.18: Thermal assessment of the chip in sunflower oil (left). TMP101 temperature sensor above and below the HIFU transmitter chip.

SUNUM. In addition, for protecting the bonding pads and thermally isolate the surface of the chip, it was buried with two-part epoxy (Henkel Pattex). Fig. 5.17 illustrates the PCB and the mentioned steps.

Table 5-2: Thermal parameters used in the simulation

Material	Thermal Conductivity (W/mK)	Specific Heat (Joule/kg °C)	Mass Density (kg/m <sup>3</sup> )
Cu	385	385	8920
FR4	0.3	950	1800
Sunflower oil	0.168	2200	920
Two-part epoxy (mixed)	0.1	1250	1100

Two TMP101 digital temperature sensors with I<sup>2</sup>C interface are placed on the epoxy coated area over the chip and under the pcb directly on the heatsink area. The thickness of epoxy layer above the chip is around 1 mm. Temperature data were recorded by Arduino nano board when the chip was ON for 100 seconds with 350 mW power consumption (since the CMUT device was at zero bias, we can account the dissipated power to be almost the same as consumed power) following by a 100 second OFF period.

Fig. 5.18 shows the setup for measurement in sunflower oil. As can be seen in Fig. 5.19, ANSYS simulation and experimental results verify each other with less than 1 °C error.

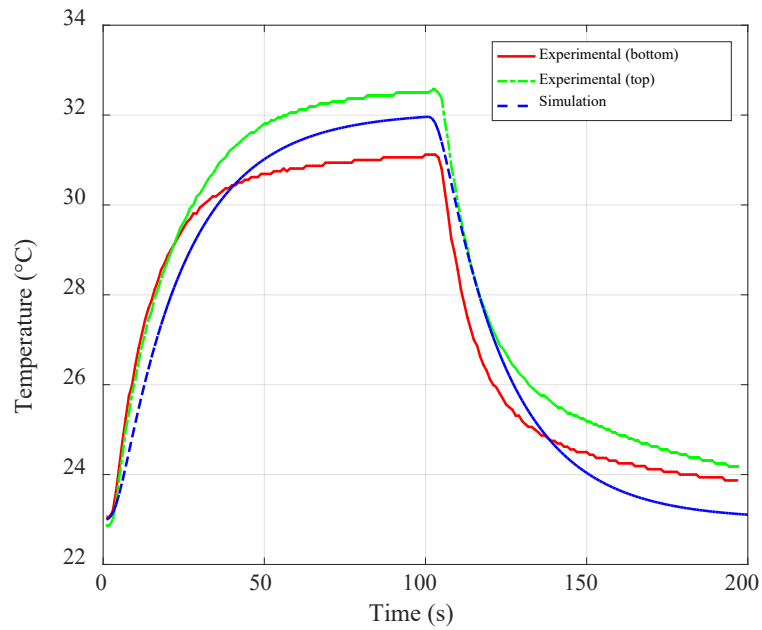


Figure 5.19: Experimental and FEM simulation results of temperature transient at the probe surface while the IC is dissipating 350 mW power. The green line corresponds to the temperature on the heatsink rod of copper.

## Chapter 6

### CONCLUSION AND FUTURE WORK

In this study the prototype of a CMUT-based fully integrated HIFU catheter system was presented. For this device two functional transmitter ICs with different transmit beamformer were fabricated. We showed that an efficient driving circuitry beside CMUT device play the important role in the functionality of the system. As one of the limiting factors in using of the HIFU catheters is the self-heating of the probe surface in body which should be kept under 42 °C as a rule of FDA. Presented transmitter ICs operate in 8-12 MHz range capable of producing 15-50 V HV driving signals for an 8-element CMUT array. Measurement results of dissipated power of chips were around 480 mW for driving of CMUT arrays at 12 MHz. Our FEM simulation results, IR thermography and experimental verifications confirm that the surface of the presented device stays in the safe temperature range during the period of delivering 600 CEM<sub>43</sub> to ovine liver in Ex-vivo experiment.

The system block diagrams in Fig. 3.1 or Fig. 3.2 reveal that the integrated system has a cable count of 8, which may be the same number even for larger number of arrays. Consequently, one may argue the necessity of all the complex circuitry for an integrated HIFU driver, and not replacing it with an external driver. One important advantage of the

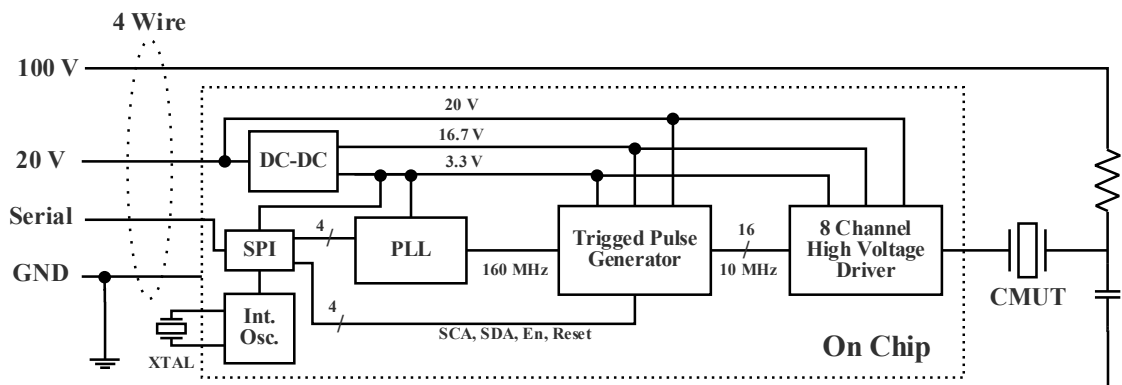


Figure 6.1: A possible scheme for reducing the number of cables to be run along the catheter.

integrated system, even when it has the same number of cables, is in the replacement of relatively expensive coaxial cables with mere power cables and a simple low rate data cable for which signal integrity is simple to achieve. The cable count can be further decreased by incorporating some functional blocks to the driver IC. These include an RS-232 interface to implement a single wire asynchronous link, and DC-DC converters for the local generation of the (relatively low current) 3.3 Volt and HVSS supply rails. A conceptual drawing of the proposed cable reduction scheme is shown in Fig. 6.1.

## REFERENCES

- [1] Khokhlova T.D., Hwang J.H. (2016) “HIFU for Palliative Treatment of Pancreatic Cancer.” In: Escoffre JM., Bouakaz A. (eds) Therapeutic Ultrasound. Advances in *Experimental Medicine and Biology*, vol 880. Springer, Cham.
- [2] Livraghi, Tito, Luigi Solbiati, M Franca Meloni, G Scott Gazelle, Elkan F Halpern, and S Nahum Goldberg. “Treatment of Focal Liver Tumors with Percutaneous Radio-Frequency Ablation: Complications Encountered in a Multicenter Study.” *Radiology* 226, no. 2 (2003): 441-51.
- [3] Costello, AJ, WG Bowsher, DM Bolton, KG Braslis, and J Burt. “Laser Ablation of the Prostate in Patients with Benign Prostatic Hypertrophy.” *BJU International* 69, no. 6 (1992): 603-08.
- [4] Labonte, Sylvain, Angeline Blais, Stéphane R Legault, Hassan O Ali, and Langis Roy. “Monopole Antennas for Microwave Catheter Ablation.” *IEEE transactions on microwave theory and techniques* 44, no. 10 (1996): 1832-40.
- [5] E. Constanciel *et al.*, “Design and evaluation of a transesophageal HIFU probe for ultrasound-guided cardiac ablation: simulation of a HIFU mini-maze procedure and preliminary ex vivo trials,” in *IEEE Transactions on Ultrasonics, Ferroelectrics, and Frequency Control*, vol. 60, no. 9, pp. 1868-1883, Sep. 2013.
- [6] T. Li, T. Khokhlova, E. Maloney, Y.-N.Wang, S.DAndrea, F. Starr, N. Farr, K. Morrison, G. Keilman, and J. H. Hwang, “Endoscopic high-intensity focused us: Technical aspects and studies in an in-vivo porcine model (with video),” *Gastrointestinal Endoscopy*, vol. 81, no. 5, pp. 1243–1250, 2015.
- [7] K. Yokoyama, H. Nakagawa, K. A. Seres, E. Jung, J. Merino, Y. Zou, A. Ikeda, J. V. Pitha, R. Lazzara, and W. M. Jackman, “Canine model of esophageal injury and atrial-esophageal fistula after applications of forward-firing high-intensity focused ultrasound and side-firing unfocused ultrasound in the left atrium and inside the pulmonary veinclinical perspective,” *Circulation, Arrhythmia Electrophysiol.*, vol. 2, no. 1, pp. 41–49, 2009.

- [8] S. N. Narouze, “Atlas of ultrasound-guided procedures in interventional pain management,” *Atlas Ultrasound-Guided Proced. Interv. Pain Manag.*, pp. 1–372, 2011.
- [9] G. Ter Haar and C. Coussios, “High intensity focused ultrasound: Physical principles and devices,” *Int. J. Hyperthermia*, vol. 23, no. 2, pp. 89–104, 2007.
- [10] Bamber J, ter Haar GR, Hill C. “Physical Principles of medical Ultrasound.” 2nd ed. London: Wiley; 2004.
- [11] M. R. Bailey, V. A. Khokhlova, O. A. Sapozhnikov, S. G. Kargl, and L. a. Crum, “Physical mechanisms of the therapeutic effect of ultrasound (a review),” *Acoust. Phys.*, vol. 49, no. 4, pp. 369–388, 2003.
- [12] Laugier, Pascal, and Guillaume Haiat. “Introduction to the Physics of Ultrasound.” In *Bone Quantitative Ultrasound*, edited by Pascal Laugier and Guillaume Haiat, 29-45. Dordrecht: Springer Netherlands, 2011.
- [13] G. S. Kino, *Acoustic Waves: Devices, Imaging, and Analog Signal Processing*. New York, NY, USA: Prentice-Hall, 1987.
- [14] Hoskins, P., A. Thrush, K. Martin, and T. Whittingam. *Diagnostic Ultrasound: Physics and Equipment*. Greenwich Medical Media, 2003.
- [15] S. A. Sapareto and W. C. Dewey, “Thermal dose determination in cancer therapy,” *Int. J. Radiation Oncology Biology Phys.*, vol. 10, no. 6, pp. 787–800, 1984.
- [16] M. W. Dewhurst, B. L. Vigiante, M. Lora-Michiels, M. Hanson, and P. J. Hoopes, “Basic principles of thermal dosimetry and thermal thresholds for tissue damage from hyperthermia,” *Int. J. Hyperthermia*, vol. 19, no. 3, pp. 267–294, 2003.
- [17] G. C. Van Rhoon, T. Samaras, P. S. Yarmolenko, M. W. Dewhurst, E. Neufeld, and N. Kuster, “CEM43 °C thermal dose thresholds: A potential guide for magnetic resonance radiofrequency exposure levels?” *Eur. Radiology*, vol. 23, no. 8, pp. 2215–2227, 2013.
- [18] O'Neill, Brian E., Howard Vo, Mary Angstadt, King P. C. Li, Tim Quinn, and Victor Frenkel. “Pulsed High Intensity Focused Ultrasound Mediated Nanoparticle Delivery: Mechanisms and Efficacy in Murine Muscle.” *Ultrasound in Medicine and Biology* 35, no. 3 (2009): 416-24.
- [19] Kim, Y., Rhim, H., Choi, M.J., Lim, H.K., & Choi, D. (2008). “High-Intensity Focused Ultrasound Therapy: an Overview for Radiologists.” *Korean journal of radiology*.

- [20] K. L. Gentry and S. W. Smith, "Integrated catheter for 3-D intracardiac echo cardiography and ultrasound ablation," *IEEE Trans. Ultrason., Ferroelectr., Freq. Control*, vol. 51, no. 7, pp. 800–808, Jul. 2004.
- [21] N. McDannold, G. Clement, P. Black, F. Jolesz, and K. Hynynen, "Transcranial MRI-guided focused ultrasound surgery of brain tumors: Initial findings in three patients," *Neurosurgery*, vol. 66, no. 2, pp. 323–332, 2010.
- [22] B. Asuri, "Active thermal management for ultrasound catheter probe," U.S. Patent US 11/715 768, 2007.
- [23] E. Brunner, "Ultrasound system considerations and their impact on frontend components," *Analog Devices*, pp. 36–03, 2002.
- [24] W. C. Black and D. N. Stephens, "CMOS chip for invasive ultrasound imaging," *IEEE J. Solid-State Circuits*, vol. 29, no. 11, pp. 1381–1387, Nov. 1994.
- [25] A. Nikoozadeh, D. J. Wygant, D. S. Lin, O. Oralkan, A. S. Ergun, D. N. Stephens, K. E. Thomenius, A. M. Dentinger, D. Wildes, G. Akopyan, K. Shivkumar, A. Mahajan, D. J. Sahn, and B. T. Khuri-yakub, "Forward looking intracardiac ultrasound imaging using a 1-D CMUT array integrated with custom front-end electronics," *IEEE Trans. Ultrason., Ferroelectr., Freq. Control*, vol. 55, no. 12, pp. 2651–2660, Dec. 2008.
- [26] G. Gurun, C. Tekes, J. Zahorian, T. Xu, S. Satir, M. Karaman, J. Hasler, and F. L. Degertekin, "Single-chip CMUT-on-CMOS front-end system for real-time volumetric IVUS and ICE imaging," *IEEE Trans. Ultrason., Ferroelectr., Freq. Control*, vol. 61, no. 2, pp. 239–250, Feb. 2014.
- [27] T. Yan, "Integrated water cooling for HIFU prostate ablation," M.Sc. thesis, TU Delft, Delft University of Technology, 2011.
- [28] G. Gurun, "Integrated electronics design for high-frequency intravascular ultrasound imaging," Ph. D. dissertation, Electrical and Computer Eng., Georgia Institute of Technology, Atlanta, GA, USA, 2011.
- [29] Farhanieh, Omid, Ali Sahafi, Rupak Bardhan Roy, Arif Sanli Ergun, and Ayhan Bozkurt. "Integrated Hifu Drive System on a Chip for Cmut-Based Catheter Ablation System." *IEEE Transactions on Biomedical Circuits and Systems* 11, no. 3 (2017): 534-46.
- [30] <http://www.theraclion.com/echopulse/product-data/>

- [31] "FOCAL THERAPY IS THE FUTURE - Have you considered HIFU?" SonaCare Medical. <http://sonacaremedical.com/index.php/surgeons/our-products/sonablate-ablation-tool>.
- [32] EDAP TMS - Leader in therapeutic ultrasound - Develops minimally-invasive therapeutic solutions for urology. Ablatherm HIFU. <https://www.edap-tms.com/en/products-services/prostate-cancer/ablatherm-hifu#prettyPhoto>.
- [33] "Laparoscopic HIFU Surgical Ablation System." SonaCare Medical. <http://sonacaremedical.com/index.php/surgeons/our-products/sonatherm>.
- [34] Salgaonkar, Vasant A., and Chris J. Diederich. "Catheter-Based Ultrasound Technology for Image-Guided Thermal Therapy: Current Technology and Applications." *International Journal of Hyperthermia* 31, no. 2 (2015/02/17 2015): 203-15.
- [35] Partanen A, Yerram NK, Trivedi H, Dreher MR, Oila J, Hoang AN, et al. "Magnetic resonance imaging (MRI)-guided transurethral ultrasound therapy of the prostate: a preclinical study with radiological and pathological correlation using customized MRI-based moulds." *BJU international*. 2013; 112(4):508–516.
- [36] Canney MS, Chavrier F, Tsysar S, Chapelon JY, Lafon C, Carpentier A. "A multi-element interstitial ultrasound applicator for the thermal therapy of brain tumors." *The Journal of the Acoustical Society of America*. 2013; 134(2):1647–1655.
- [37] Makin IRS, Mast TD, Faidi W, Runk MM, Barthe PG, Slayton MH. "Miniaturized ultrasound arrays for interstitial ablation and imaging." *Ultrasound in medicine & biology*. 2005; 31(11):1539–1550.
- [38] Natale A, Pisano E, Shewchik J, Bash D, Fanelli R, Potenza D, et al. "First human experience with pulmonary vein isolation using a through-the-balloon circumferential ultrasound ablation system for recurrent atrial fibrillation." *Circulation*. 2000; 102(16):1879–1882.
- [39] Wootton JH, Hsu ICJ, Diederich CJ. "Endocervical ultrasound applicator for integrated hyperthermia and HDR brachytherapy in the treatment of locally advanced cervical carcinoma." *Medical physics*. 2011; 38(2):598–611
- [40] V.M.D.Nascimento and V. L. Button, "Influence of backing and matching layers in ultrasound transducer performance," in *Ultrasonic Imaging and Signal Processing, Proc. SPIE*, vol. 5035, 2003, Conference Proceedings, pp. 86–96.
- [41] X. Zhuang, B. T. Khuri-Yakub, G. G. Yaralioglu, M. Kupnik, O. Oralkan, S. H. Wong, A. S. Ergun, and K. Butts-Pauly, "Capacitive micromachined ultrasonic

- transducers for high intensity focused ablation of upper abdominal tumors,” in *Proc. IEEE Ultrasonics Symp.*, Oct. 2006, pp. 841–844.
- [42] A. S. Ergun, S. Barnes, and E. Gardner, “An assessment of the thermal efficiency of capacitive micromachined ultrasonic transducers,” in *Proc. IEEE Ultrasonics Symp.*, Oct. 2007, pp. 420–423.
- [43] H.T. Soh and I. Ladabaum. Silicon micromachined ultrasonic immersion transducers.  
Applied Physics Letters, 69(24):3674-3676, 1996.
- [44] R. Bardhan Roy, O. Farhanieh, A. S. Ergün and A. Bozkurt, "Fabrication of High-Efficiency CMUTs With Reduced Parasitics Using Embedded Metallic Layers," in *IEEE Sensors Journal*, vol. 17, no. 13, pp. 4013-4020, July 1, 2017.
- [45] Köhler, Max Oskar, Peter Dirksen, Shunmugavelu Sokka, and Ronald Dekker. “Catheter Comprising Capacitive Micromachined Ultrasonic Transducers with an Adjustable Focus.” Google Patents, 2014.
- [46] W. A. N’Djin *et al.*, "Capacitive Micromachined Ultrasound Transducers for Interstitial High-Intensity Ultrasound Therapies," in *IEEE Transactions on Ultrasonics, Ferroelectrics, and Frequency Control*, vol. 64, no. 8, pp. 1245-1260, Aug. 2017.
- [47] J. H. Jang *et al.*, "Integration of a dual-mode catheter for ultrasound image guidance and HIFU ablation using a 2-D CMUT array," *2017 IEEE International Ultrasonics Symposium (IUS)*, Washington, DC, 2017, pp. 1-4.
- [48] N. M. Tole and H. Ostensen, *Basic Physics of Ultrasonographic Imaging*. World Health Organization, 2005.
- [49] A. Bozkurt, R. B. Roy, and S. Ergun, “Optimization of operating frequency of acoustic transducers for obtaining maximum temperature in hifu based therapeutic ablation,” in *Proc. IEEE Int. Ultrasonics Symp.*, Oct. 2012, pp. 1–4.
- [50] H. Yetik, C. Ariyurek, A. Bozkurt, and A. S. Ergun, “Frequency optimization in high intensity focused ultrasound,” in *Proc. IEEE Int. Ultrasonics Symp.*, Sep. 2014, pp. 409–412.
- [51] R. E. Caulfield, X. Yin, J. Juste, and K. Hynynen, “A novel phase assignment protocol and driving system for a high-density focused ultrasound array,” *IEEE Trans. Ultrason., Ferroelectr., Freq. Control*, vol. 54, no. 4, pp. 793–801, Apr. 2007.

- [52] O. Oralkan, "Acoustical imaging using capacitive micromachined ultrasonic transducer arrays: Devices, circuits, and systems," Ph.D. dissertation, Dept. Electr. Eng., Stanford Univ., Stanford, CA, USA, 2004.
- [53] K. Chen, H. S. Lee, A. P. Chandrakasan, and C. G. Sodini, "Ultrasonic imaging transceiver design for CMUT: A three-level 30-V<sub>pp</sub> pulse shaping pulser with improved efficiency and a noise-optimized receiver," *IEEE J. Solid-State Circuits*, vol. 48, no. 11, pp. 2734–2745, Nov. 2013.
- [54] F. Prat, C. Lafon, J. Margonari, F. Gorry, Y. Theillre, J.-Y. Chapelon, and D. Cathignol, "A high-intensity us probe designed for intraductal tumor destruction: Experimental results," *Gastrointestinal Endoscopy*, vol. 50, no. 3, pp. 388–392, 1999.
- [55] S. H. Wong, M. Kupnik, R. D. Watkins, K. Butts-Pauly, and B. T. Khuri-Yakub, "Capacitive micromachined ultrasonic transducers for therapeutic ultrasound applications," *IEEE Trans. Biomed. Eng.*, vol. 57, no. 1, pp. 114–123, Jan. 2010.
- [56] M. Wang, J. Chen, X. Cheng, J.-C. Cheng, and P.-C. Li, "Design and test of a monolithic ultrasound-image-guided HIFU device using annular CMUT rings," in *Proc. IEEE Ultrasonics Symp.*, Nov. 2008, pp. 459–462.
- [57] J. H. Jang, M. F. Rasmussen, A. Bhuyan, H. S. Yoon, A. Moini, C. Chang, R. D. Watkins, J. W. Choe, A. Nikoozadeh, D. Stephens, O. Oralkan, K. B. Pauly, and B. Khuri-Yakub, "Dual-mode integrated circuit for imaging and HIFU with 2-D CMUT arrays," in *Proc. IEEE Int. Ultrasonics Symp.*, Oct. 2015, pp. 1–4.
- [58] Z. Gao, P. Gui, and R. Jordanger, "An integrated high-voltage low distortion current-feedback linear power amplifier for ultrasound transmitters using digital predistortion and dynamic current biasing techniques," *IEEE Trans. Circuits Syst. II, Exp. Briefs*, vol. 61, no. 6, pp. 373–377, Jun. 2014.
- [59] W. T. Ang, C. Scurtescu, W. Hoy, T. El-Bialy, Y. Y. Tsui, and J. Chen, "Design and implementation of therapeutic ultrasound generating circuit for dental tissue formation and tooth-root healing," *IEEE Trans. Biomed. Circuits Syst.*, vol. 4, no. 1, pp. 49–61, Feb. 2010.
- [60] M. Bechtold, B. Granz and R. Oppelt, "A 2-D acoustic array for diagnostic imaging," *1996 IEEE Ultrasonics Symposium. Proceedings*, San Antonio, TX, 1996, pp. 1573-1576 vol.2.
- [61] R. Chanamai and D. J. McClements, "Ultrasonic attenuation of edible oils," *J. Amer. Oil Chemists' Soc.*, vol. 75, no. 10, pp. 1447–1448, 1998.

- [62] O. Fasina and Z. Colley, "Viscosity and specific heat of vegetable oils as a function of temperature: 35 °C to 180 °C," *Int. J. Food Properties*, vol. 11, no. 4, pp. 738–746, 2008.
- [63] B. Razavi, *RF Microelectronics*. New York, NY, USA: Prentice Hall, 2010, vol. 2.
- [64] X. Zhao, R. Chebli, and M. Sawan, "A wide tuning range voltage controlled ring oscillator dedicated to ultrasound transmitter," in *Proc. 16th Int. Conf. Microelectronics*, Dec. 2004, pp. 313–316.
- [65] N. Sun, T. J. Yoon, H. Lee, W. Andress, R. Weissleder, and D. Ham, "Palm NMR and 1-chip NMR," *IEEE J. Solid-State Circuits*, vol. 46, no. 1, pp. 342–352, Jan. 2011.
- [66] J. Kim, B. Hammer, and R. Harjani, "A 5–300 MHz CMOS transceiver for multi-nuclear NMR spectroscopy," in *Proc. IEEE Custom Integrated Circuits Conf.*, Sep. 2012, pp. 1–4.
- [67] M. K. Mandal and B. C. Sarkar, "Ring oscillators: Characteristics and applications," *Indian J. Pure Applied Phys.*, vol. 48, pp. 136–145, 2010.
- [68] A. Hajimiri, S. Limotyrakis, and T. H. Lee, "Jitter and phase noise in ring oscillators," *IEEE J. Solid-State Circuits*, vol. 34, no. 6, pp. 790–804, Jun. 1999.
- [69] W. Rhee, "Design of high-performance CMOS charge pumps in phase locked loops," in *Proc. IEEE Int. Symp. Circuits and Systems*, vol. 2, Jul. 1999, pp. 545–548.
- [70] C.-L. Ti, Y.-H. Liu, and T.-H. Lin, "A 2.4-GHz fractional-N PLL with a PFD/CP linearization and an improved CP circuit," in *Proc. IEEE Int. Symp. Circuits and Systems*, May 2008, pp. 1728–1731.
- [71] C. S. Vaucher, I. Ferencic, M. Locher, S. Sedvallson, U. Voegeli, and Z. Wang, "A family of low-power truly modular programmable dividers in standard 0.35  $\mu\text{m}$  CMOS technology," *IEEE J. Solid-State Circuits*, vol. 35, no. 7, pp. 1039–1045, Jul. 2000.
- [72] A. Sahafi, J. Sobhi, M. Sahafi, O. Farhanieh, and Z. D. Koozehkanani, "Ultra low power frequency divider for 2.45 GHz zigbee frequency synthesizer," *Anal. Integr. Circuits Signal Process.*, vol. 74, no. 1, pp. 97–103, 2013.
- [73] P. Behnamfar, R. Molavi, and S. Mirabbasi, "Transceiver design for CMUT-based super-resolution ultrasound imaging," *IEEE Trans. Biomed. Circuits Syst.*, vol. 10, no. 2, pp. 383–393, Apr. 2016.

- [74] H.-K. Cha, D. Zhao, J. H. Cheong, B. Guo, H. Yu, and M. Je, "A CMOS high-voltage transmitter IC for ultrasound medical imaging applications," *IEEE Trans. Circuits Syst. II: Exp. Briefs*, vol. 60, no. 6, pp. 316–320, Jun. 2013.
- [75] R. Chebli and M. Sawan, "Fully integrated high-voltage front-end interface for ultrasonic sensing applications," *IEEE Trans. Circuits Syst. I, Reg. Papers*, vol. 54, no. 1, pp. 179–190, Jan. 2007.
- [76] J. G. Maneatis, "Low-jitter process-independent DLL and PLL based on self-biased techniques," in *IEEE Journal of Solid-State Circuits*, vol. 31, no. 11, pp. 1723-1732, Nov 1996.
- [77] Keliu Shu, E. Sanchez-Sinencio, J. Silva-Martinez and S. H. K. Embabi, "A 2.4-GHz monolithic fractional-N frequency synthesizer with robust phase-switching prescaler and loop capacitance multiplier," in *IEEE Journal of Solid-State Circuits*, vol. 38, no. 6, pp. 866-874, June 2003.
- [78] A. A. Abidi, "Phase noise and jitter in CMOS ring oscillators," *IEEE J. Solid-State Circuits*, vol. 41, no. 8, pp. 1803–1816, Aug. 2006.
- [79] S. H. Wong, R. D. Watkins, M. Kupnik, K. B. Pauly, and B. T. Khuri-Yakub, "Feasibility of MR-temperature mapping of ultrasonic heating from a CMUT," *IEEE Trans. Ultrason., Ferroelectr., Freq. Control*, vol. 55, no. 4, pp. 811–818, Apr. 2008.
- [80] Y.-S. Hsiao, "Focused ultrasound thermal therapy monitoring using ultrasound, infrared thermal, and photoacoustic imaging techniques," Ph.D. dissertation, Univ. Michigan, Ann Arbor, MI, USA, 2013.
- [81] "IR Window Transmission Guidebook", CorDEX Instrument, ID 4015 Rev A.
- [82] K.-D. Gruner, "Principles of non-contact temperature measurement," 2003, RAYTEK GmbH.
- [83] R. P. Madding, "Infrared window transmittance temperature dependence," 2004, Infrared Training Center. FLIR Systems, Inc.
- [84] D. Haemmerich, J. G. Webster, and D. M. Mahvi, "Thermal dose versus isotherm as lesion boundary estimator for cardiac and hepatic radiofrequency ablation," in *Proc. 25th Annu. Int. Conf. IEEE Engineering in Medicine and Biology Soc.*, vol. 1, Sep. 2003, pp. 134–137.
- [85] H. S. Yoon, C. Chang, J. H. Jang, A. Bhuyan, J.W. Choe, A. Nikoozadeh, R. Watkins, D. Stephens, K. B. Pauly, and B. Khuri-Yakub, "Ex-vivo HIFU

experiments using a  $32 \times 32$ -element CMUT array,” *IEEE Trans. Ultrason., Ferroelectr., Freq. Control*, vol. 63, no. 12, pp. 2150–2158, Dec. 2016.